Multiscale investigations of the degradation progress in the localised fracture zone of carbon short-fibre reinforced high-performance concrete subjected to high-cycle tensile and flexural fatigue load regimes

Oliver Fischer, Dirk Volkmer, Christian U. Grosse, Malte A. Peter, Philipp Lauff, Ante Džolan, Roland Niedermeier, Matthias Rutzen, Michael Engelhard, Polina Pugacheva, Manuel Raith, Ursula Weiss, Tanja Lochner

Angaben zur Veröffentlichung / Publication details:

Fischer, Oliver, Dirk Volkmer, Christian U. Grosse, Malte A. Peter, Philipp Lauff, Ante Džolan, Roland Niedermeier, et al. 2026. "Multiscale investigations of the degradation progress in the localised fracture zone of carbon short-fibre reinforced high-performance concrete subjected to high-cycle tensile and flexural fatigue load regimes." In *Cyclic deterioration of high-performance concrete: reports of the SPP 2020 Experimental-Virtual-Lab*, edited by Nadja Oneschkow and Ludger Lohaus, 305–44. Cham: Springer. https://doi.org/10.1007/978-3-032-19394-0_15.

Multiscale Investigations of the Degradation Progress in the Localised Fracture Zone of Carbon Short-Fibre Reinforced High-Performance Concrete Subjected to High-Cycle Tensile and Flexural Fatigue Load Regimes

Oliver Fischer, Dirk Volkmer, Christian U. Grosse, Malte A. Peter, Philipp Lauff, Ante Džolan, Roland Niedermeier, Matthias Rutzen, Michael Engelhard, Polina Pugacheva, Manuel Raith, Ursula Weiss, and Tanja Lochner

Abstract The complex mechanisms leading to degradation of a 3D-printed carbon short-fibre reinforced high-performance concrete which—due to the orientation of the carbon fibres—achieves very high tensile and flexural strengths, are investigated. For this purpose, multiple measurement methods acting on different scales were combined. At macro level, acoustic emission analysis and coda wave interferometry were used in cyclic, uniaxial tensile tests alongside conventional measurement methods such as digital image correlation to visualise internal damage. In addition, conductivity of the carbon fibres enabled conclusions to be drawn about the damage by measuring electric resistances. At micro and meso scale, the microstructure of unloaded specimens and development of microcracks were recorded in bending and

O. Fischer (✉) · P. Lauff · A. Džolan · R. Niedermeier
Chair of Concrete and Masonry Structures, Technical University of Munich (TUM), Munich, Germany
e-mail: oliver.fischer@tum.de

D. Volkmer · M. Rutzen · M. Engelhard
Chair of Solid State and Materials Chemistry, Institute of Physics, University of Augsburg (UNA), Augsburg, Germany

C. U. Grosse · P. Pugacheva · M. Raith
Chair of Non-Destructive Testing (NDT), Technical University of Munich (TUM), Munich, Germany

M. A. Peter · U. Weiss
Centre for Advanced Analytics and Predictive Sciences (CAAPS), University of Augsburg (UNA), Augsburg, Germany

M. A. Peter · T. Lochner
Institute of Mathematics, University of Augsburg (UNA), Augsburg, Germany

N. Oneschkow and L. Lohaus (eds.), *Cyclic Deterioration of High-Performance Concrete*, https://doi.org/10.1007/978-3-032-19394-0_15

in tension tests utilising computer tomography and microscopic examinations. Based on measurement data, microstructure-orientated unit cells allowing for the development of microcracks were derived and integrated into a computational homogenisation scheme capable of reproducing the material behaviour and relevant failure mechanisms.

Keywords Carbon short-fibre reinforced concrete · Oriented fibres · Multiscale fatigue testing and modelling · Degradation · Localisation of failure · NDT methods

1 Introduction

The extrusion of a carbon short-fibre reinforced mortar paste through a small nozzle leads to the fibres being aligned in the direction of the material flow (i.e. the direction of movement of the printing nozzle). This fact can be utilised to adjust the fibre orientation with the main tensile trajectories and thus to an anticipated loading scenario. In previous research, this concept has been proven to be very effective and that cementitious composite specimens can be produced with outstanding tensile and flexural strength, e.g. [1, 2]. Having also shown that up-scaling—starting from small cementitious samples (micro-scale)—to a carbon short-fibre reinforced concrete (CSFRC) is possible [3, 4], a very versatile high-performance material is available which will be investigated experimentally and theoretically with regard to high-cycle fatigue under different types/levels of loading as well as in terms of damage development, failure mechanisms and localisation.

1.1 General Research Procedure

One main objective was to gain new in-depth insights into the damage behaviour and the main failure mechanisms of the CSFRC material under different loading regimes (static, cyclic, variable) by means of experimental investigations using centric tensile as well as 3-point bending tests on different scales (micro, meso and macro specimens) and to be able to interpret and compare the scale levels. While the micro specimens offer advantages for analytics and are easier to access for mathematical simulations, meso-size samples have particularly proven suitable for AE methods and correlations with LDV. Large-scale experiments that are closer to real-life applications, are essential for identifying potential scale effects and also offer advantages for various measurement techniques such as electrical and fibre-optical methods or DIC. On the basis of the extensive test and measurement results gained from the project, suitable mathematical models were derived representing the damage and failure mechanisms as realistically as possible while remaining computationally feasible with standard commercial software packages. Modelling and simulation initially starts at micro level and with static loads and consequently aims to predict experimental results derived with macro samples as well as under dynamic fatigue loading and to calibrate the models accordingly.

While the focus of the experimental investigations was firstly laid on simple static and monotonic tests (performed on micro 3-point bending and macro tensile specimens) as well as on identifying, generally assessing and evaluating the complex damage and failure mechanisms of CSFRC and the establishment of suitable measuring technologies, later the focus was laid on scale transition (micro tensile, macro/meso 3-point bending specimens) and the extension to more complex fatigue loads, more refined measurements and the combination of different sensor techniques.

1.2 Material, Testing Specimens

Following previous investigations, carbon short-fibres (CSF) with 7 μm in diameter and a length of 3 mm were utilised as "reinforcement" of the cementitious material after desizing and oxidation of the fibre surface, please refer to e.g. [1, 2, 5]. Hereby, two types of fibres were used, Tenax-J HT C261 carbon fibres (for micro and most of the meso samples) and Zoltek (Toray) PX35 fibres (macro samples). Regarding the concrete mix, for the micro samples a suitable concrete paste was deployed being already investigated for several years to achieve optimum extrudability and fibre dispersion in the 3D-printing process of small-scale samples [1]: 61.0 weight percent (wt.%) Schwenk CEM I 52.5 R, 21.0 wt.% EFACO silica fume, 3.0 wt.% superplasticiser BASF ACE 430 and 15.0 wt.% of water (w/o aggregates). The concrete mix design for the meso/macro specimens was composed of 34.7 wt.% Holcim Sulfo 52.5 R cement, 21.7 wt.% Sika Silicol P fume, 21.7 wt.% quartz powder SF 500, 7.7 wt.% quartz sand, 2.5 wt.% superplasticiser ACE 460 and 11.7 wt.% of water. While the fibre content of the micro samples varied between 0 (unreinforced) and 1–3 vol.%, all meso/micro specimens had a fibre content of 1 vol.%.

Regarding the geometry of the different specimens, the macro tensile specimens (tested in uniaxial tension) had a dog-bone shape with dimensions shown in Fig. 1a, while the smaller micro and meso specimens tested in uniaxial tension had reduced dimensions (scale factor 10 and 20%). All samples tested in 3-point bending (flexural tensile strength) were prismatic with square cross-sections and the load being applied at midspan (symmetry axis). While the macro samples (bending) had a cross-section of 40 × 40 and 180 mm free span, the corresponding dimensions of the micro samples were 5 × 5 mm (span 15 mm) and those of the meso samples 15 × 15 mm (span 90 mm). For manufacturing, a special 3D printer was developed at TUM for the *macro samples* [6, 7]. Through the printing process, the desired fibre orientation was achieved both in the dog-bone shaped tension specimens (Fig. 1b, c) and the prismatic flexural samples (fibre orientation parallel to lower edges, i.e. in the direction of the principal tensile trajectories in the midspan tensile zone) (Fig. 2).

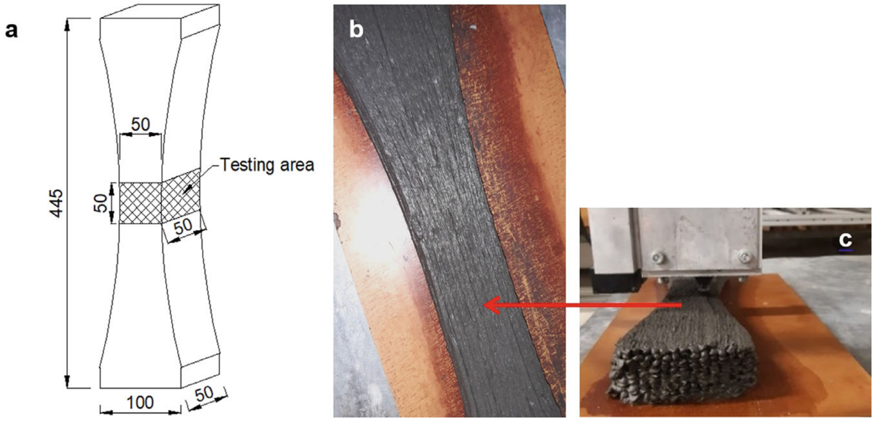

Fig. 1 Shape/dimensions (mm) of *macro specimens* tested in centric tension (**a**), 3D-printed dog-bone shaped sample (**b**) and printing process (**c**)

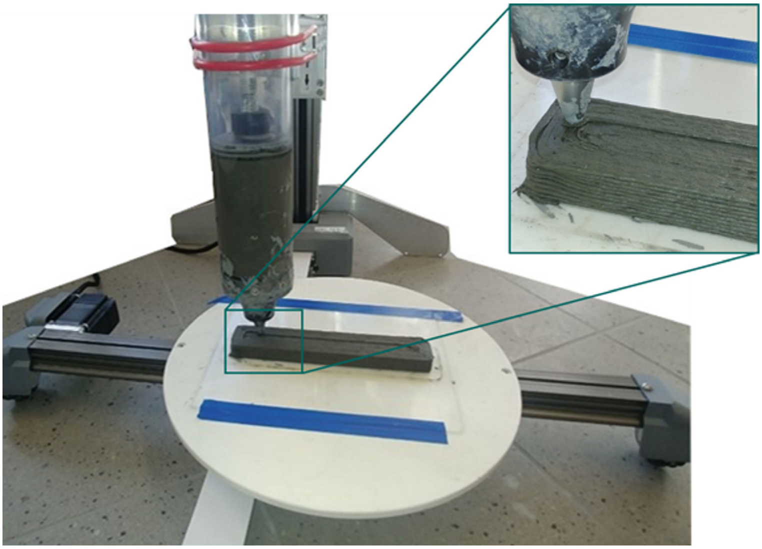

Fig. 2 3D printing of meso size flexural beam specimens with CSFRC material

2 Experimental Investigations on CSFRC Specimens

The present section firstly outlines which experimental tests were carried out with the CSFRC material, refer to Table 1. Please note that only the highly instrumented principal experiments are included therein, while numerous additional tests aiming on optimising the testing and measurement setup are not listed. It then addresses static loading tests, cyclic monotonic tests and fatigue tests with varied stress levels

Table 1 Overview: static/cyclic experimental investigations on the CSFRC material (number of highly instrumented tests performed)

Sample size	Static load	Cyclic loading (monotonous)	Cyclic loading (varied load, sequence effects)
Micro	> 60	25	–
Meso	48	10	1
Macro	30	36	26

and the analysis of sequence effects. In each case, it is specified both whether micro or macro/meso test specimens were used and if uniaxial tensile tests or 3-point bending tests were performed. Hereby, key findings from the various tests are explained and discussed directly. In addition, Sect. 3 provides a detailed summary of all the measurement techniques utilised (including their combination) and the findings that can be derived from the measuring results with regard to load-bearing behaviour, damage development, fatigue behaviour and the different failure mechanisms of the CSFRC material. Finally, Sect. 4 addresses mathematical modelling aspects and the numerical simulation of the load-bearing behaviour of the material.

2.1 *Static Loading Tests, General Behaviour of the Material*

To illustrate the general load-bearing and deformation behaviour and the significant difference to fibre-free samples, Fig. 3 illustrates typical stress–strain curves in both static tensile tests (Fig. 4) and in 3-point bending tests for different fibre content using the CSFRC micro test specimens as an example.

Micro beam specimens without reinforcement show purely linear-elastic behaviour and a flexural strength of a maximum of about 22 MPa (Fig. 3a). Addition

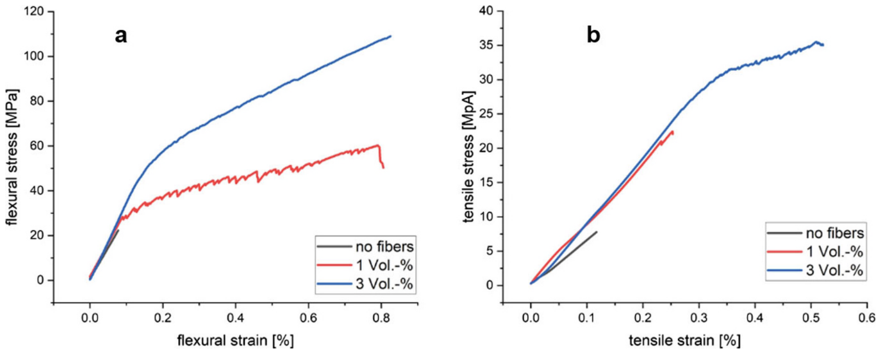

Fig. 3 Stress–strain curves with different fibre content; **a** extruded micro beam specimens (3-point bending test [8]) and **b** micro tensile test samples

of 1 volume percent (vol.%) of CSF leads to a sharp increase in flexural strength up to 60 MPa, if 3 vol.% are included in the mortar a flexural strength of the specimens of up to 110 MPa can be achieved, also see e.g. [9]. In comparison, tensile micro samples with 1 vol.% CSF achieve a uniaxial tensile strength of up to 23 MPa, while with 3 vol.% some 35 MPa of tension can be reached before failure (Fig. 3b).

Specimens reinforced with CSF show a pronounced strain-hardening behaviour. For tensile micro specimens with 1 vol.% it can be stated that the critical fibre content is not yet reached. Nevertheless, a distinct strain hardening can be observed and was therefore investigated in detail (see e.g. Sects. 3.1–3.4), because a higher fibre content would have made segmentation impossible (see Sect. 3.4, Fig. 23b) and thus, no reliable basis would have been available for the multiscale modelling (see Sect. 4). The specific deformation behaviour is linked to the CSF being able to bridge the cracks. Leaving the linear-elastic regime instantly leads to unstable crack growth (and thus to failure) in the unreinforced material, crack growth is inhibited in the fibre-reinforced specimens. As the fibres bridge the cracks, there is only a minor change in the overall tensile load transfer along the specimens which in turn causes the formation of multiple microcracks. Materials showing such a behaviour have been described and discussed in the literature since the early 1990s under the terms 'Engineered Cementitious Composites' (ECCs) or 'Strain Hardening Cementitious Composites' (SHCCs), see e.g. [10–13].

In addition to 3-point bending tests, also dog-bone shaped *micro specimens* were analysed in *static tensile tests*. The main reason for this was to ensure the feasibility of the in-situ tensile testing in the computer tomograph (refer to Sect. 3.4), which

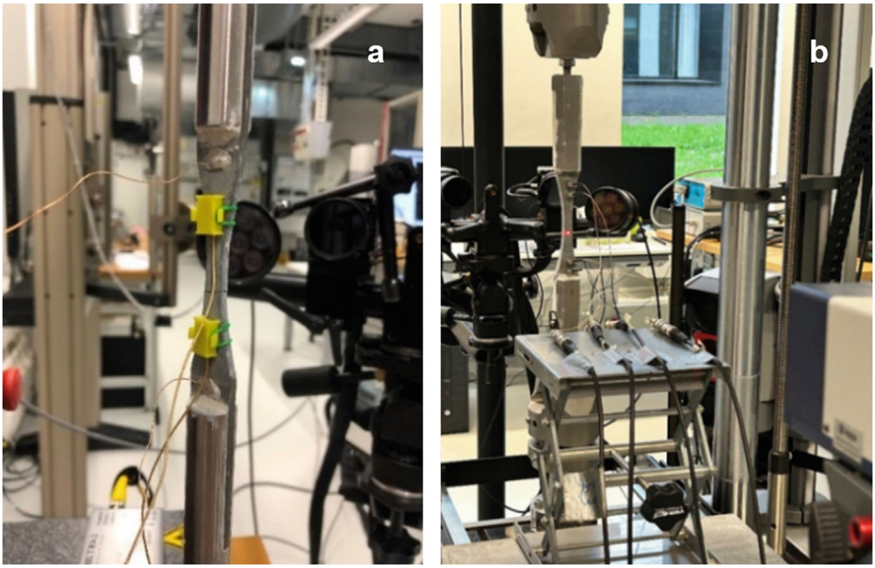

Fig. 4 Static tensile test setup on micro sized specimens

gained more insights and also facilitated a multiscale modelling (see Sect. 4). It was possible to integrate various measurement methods in-situ. Tensile tests on micro specimens were carried out using a universal testing machine with a 5 kN load cell produced by Zwick&Roell (Ulm, Germany) whereas the meso size samples were tested using an Instron (Norwood, USA) ElectroPuls E10000 testing machine.

The experiments were partly monitored by AE detectors (also see Sect. 3.3), 2D or 3D camera systems for DIC and by means of LDV. Additional measurements were performed to determine the material properties, while testing methods were improved. In this context, it has to be stated that the meso size specimens were specifically designed for investigations concerning the correlation of AE and LDV (see Sect. 3.3).

2.2 *Cyclic Tests (Monotonous)*

In the beginning, a variety of uniaxial *tensile fatigue tests* (monotonic load cycles) have been carried out with *macro specimens*, please e.g. refer to [14]. These tests were systematically accompanied utilising several measuring techniques in order to gain as much insight as possible to internal damaging mechanisms and the general fatigue process of the novel material, see e.g. [15]. In the following, test series 'E6' is discussed, which was tested at a frequency of 5 Hz, a cyclic load varying between 40 and 80% of the static tensile strength ($f_{ct} = 13.48$ MPa) and with 1 vol.% CSF. Specimen age was between 29 and 35 days at beginning of testing; the total number of load cycles (until failure) varied from 0.4 to 5.1 million.

Compared to standard concrete under fatigue loading, which exhibits three clearly distinguishable phases of damage evolution, i.e. initiation of microcracks (phase 1), stable crack growth (phase 2) and instable crack development (phase 3), CSFRC behaves differently—generally and scale-dependent (sample size). Put simply: the larger the scale, the less distinct the phases can be recognised (especially phase 3).

As can be seen in Fig. 5a (strain gauge measurement), phase 1 is very short and barely visible in tests E6.1 and E6.6. The subsequent phase 2 accounts for most of the testing time, with crack growth tending to stagnate or even 'decrease', as in test E6.6. Phase 3 is only visible in test E6.4, while samples in the other tests break more or less abruptly without any noticeable increased cracking. A closer look at test E6.4 reveals the reason for the high strain rate shortly before failure (see Fig. 6). During the load cycles, the diagram shows the evolution of strain at the respective points of maximum load with temperature compensation (index T). In this test, the crack that led to failure ran across the strain gauge DMS1U.

The strain increases rapidly as the crack reached the respective gauge at about 270,000 cycles, whereas the other strain gauges remain in their slowly increasing tendency. DMS3U is located very close to the crack, however, only a slight effect on the strain development can be seen at the end of the fatigue test. This evaluation shows that the development of microcracks is highly localised and has little effect

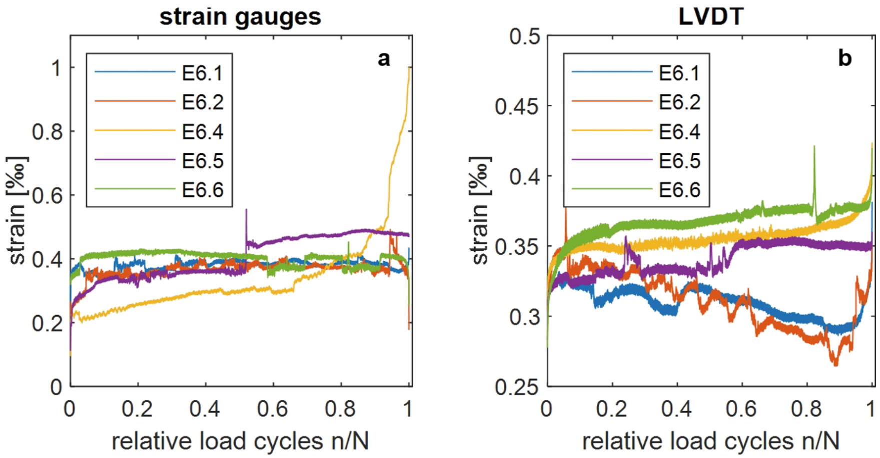

Fig. 5 Strain development during fatigue test (macro tensile samples, series E6): **a** average value from four strain gauges with virtually abrupt failure; **b** average value from three inductive displacement sensors (LVDT) measuring the strain integrally over the specimen's length

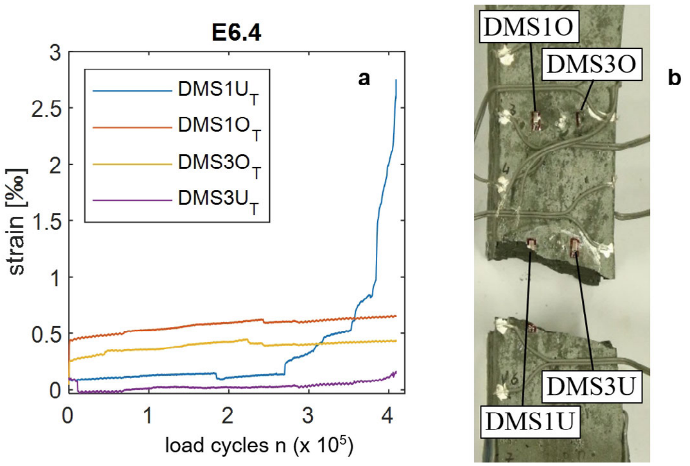

Fig. 6 Examination of individual strain gauge measurements for test E6.4 (**a**), where gauge DMS1U being located directly above the final failure crack; position of individual strain gauges with 3 mm measuring length and final crack (**b**)

on neighbouring areas. If no strain gauge crosses the microcrack leading to failure, the proximity to fracture cannot be detected.

Figure 15 shows the strain measurement with DIC for the same specimen E6.4. The gauges are located on the side opposite the speckle pattern or DIC camera, respectively (also see Fig. 15). Two areas with major damage and microcrack widening are clearly visible. The one further down in the DIC image leads to final failure. On closer inspection of this area, multiple parallel microcracks can be clearly identified, which define a small damage zone but are locally limited in the horizontal direction. Further DIC evaluations for this test (not shown here) reveal that the critical failure area formed at the beginning of the fatigue test due to the merging of several microcracks.

Looking at the results obtained with inductive displacement transducers (LVDT), measuring integrally over the entire height of the specimen, a more general trend in strain development can be observed (Fig. 5b). Almost all tests show a flattening curve in phase 1, with four tests also showing a clear transition to phase 3. The tests E6.5 and E6.6, however, fail and hence show a similar behaviour as the local strain gauge measurement without indicating phase 3. A considerable factor is the decreasing strain development in tests E6.1 and E6.2, the cause of which is still unknown.

The crack surface analysis by means of electron microscopy reveals the fact that final failure of the specimen mainly occurs due to fibre breakage, not due to fibre pull-out. This finding also fits to the size of the microcracks. Although the final failure crack is widening significantly compared to other regions of the tested sample, this crack is smaller than 100 μm and therefore is barely visible by human eyes.

In summary, it can be said that, compared to normal concrete, a basically similar fatigue behaviour is observed, but that there are significant deviations in phase 3.

In addition to monotonous tests on macro specimens, also a huge number of dynamic experiments was performed on *micro samples* subjected to *cyclic loading* in *3-point bending* tests, particularly in the first phase of the research, see e.g. [8, 9]. In the following, a typical experiment is shown with selected representative results, which are subsequently discussed.

The positive influence of the fibres again leads to an increased fatigue resistance under cyclic loads. Figure 7b shows a Woehler S–N-diagram for unreinforced micro beam specimens and those with 1 vol.% carbon fibres. For better comparability, the stress values in the diagram are normalised to the flexural strength of the respective test specimen. Specified numbers correspond to the upper load limit (i.e. 60% of the flexural strength); the lower load limits can be obtained by subtracting the selected load amplitude of 40%. The tests were carried out using a DMA testing machine with a load frequency of 100 Hz. In general, the number of cycles to failure increases by a factor of approximately 100 when comparing the micro beam specimen without fibres (which, depending on load level, typically withstands between 10^3 and 10^5 cycles until failure) with the sample containing 1 vol.% CSF (which fail after approximately 10^6–10^7 load cycles).

A more micro-structural view on the fatigue behaviour can be obtained by observing various parameters that correlate with the damage accumulated in the specimen during the load cycles. It has been shown that observation of viscoelasticity represented by Storage Modulus (SM; representing the elastic properties, similar to the Young's Modulus) and Loss Modulus (LM; representing the viscous properties and thus pointing to irreversible changes) allows for meaningful predictions. A more in-depth explanation of the significance of SM and LM during cyclic experiments is given in [16]. Figure 8 shows the development of these moduli over the duration of a fatigue test (here: upper load limit 60% of the beam's flexural strength).

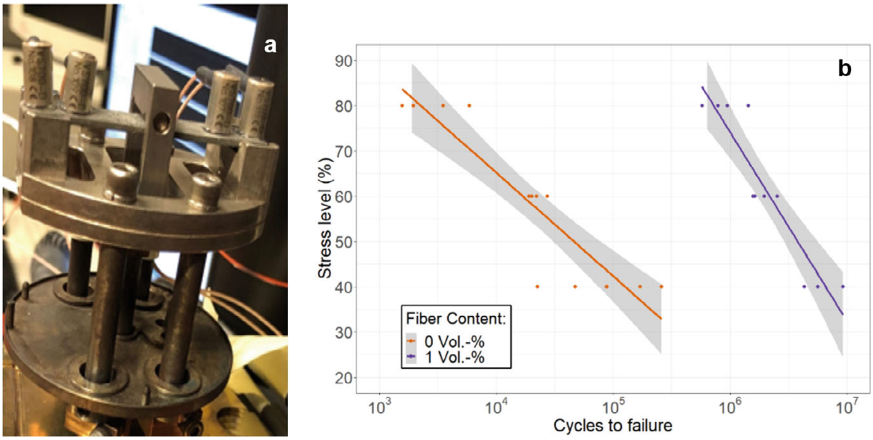

Fig. 7 Cyclic 3-point micro bending test setup within an DMA Q800, TA Instruments (**a**), Woehler diagram comparing the fatigue life of extruded micro beam specimens without fibres to those with 1 vol.% of carbon short-fibres (**b**). Adapted from [16], with modifications

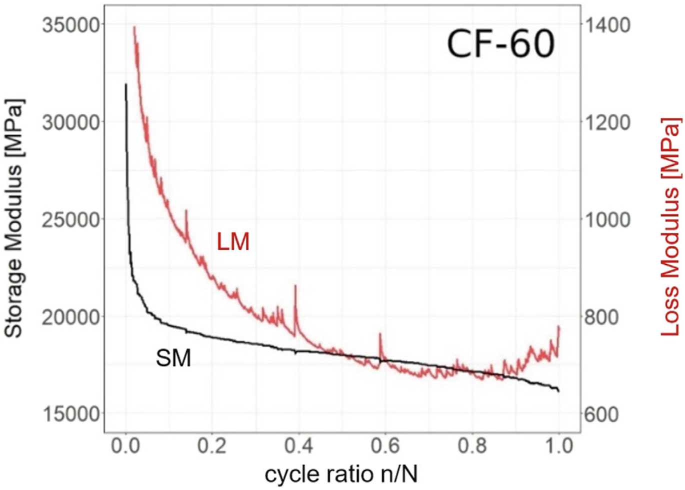

Fig. 8 Development of SM and LM during fatigue test of a CSFRC micro beam specimen (1 vol.% CSF, upper load limit 60% (i.e. load type CF-60), lower load limit 20% of flexural strength). Adapted from [16], with modifications

The moduli show a specific and repeatable pattern during the runtime of the fatigue test. SM and LM both start to fall rapidly very early, corresponding to a considerable loss in stiffness due to crack formation. After about 10% of the experiment's runtime, both moduli decrease at a steady and slow speed. Some sharp peaking in LM can be seen, indicating non-reversible inelastic events, which likely show the formation of further cracks. After some 80% of the runtime, the specimen enters a third phase of behaviour, where SM continues to decrease slightly faster while LM starts to increase again. This behaviour proved to be the indication of the end of the micro beam's fatigue life. As the increase in modulus appears quite early, it might prove a useful indicator during real-world application.

An identical experiment was carried out on another micro beam sample. Hereby, the test was interrupted at the cycle ratios indicated by dashed lines in Fig. 8 and an X-ray CT scan was performed to assess the damage caused by the cyclic loading. The results can be seen in Sect. 3.4 (refer to e.g. Figure 24). The scanned area shows a length of some 7 mm, taken at the midspan area of the beam thus representing the location subjected to the highest bending moment. Since several AE sensors were attached to the surface of the sample, it was also possible to correlate the AE activity (see Sect. 3.3) with the specimen's mechanical behaviour.

2.3 Advanced Cyclic Tests (Varied Loading, Sequence Effects)

Tensile and flexural tests were mainly performed with macro samples (please refer to Table 1) using four different schemes of cyclic loading in order to investigate sequence effects by varied loading. These schemes are described in Table 2 and schematically shown in Fig. 9 for load type 1. Hereby, the background colours for the individual load levels are also used in Fig. 10. The concrete stresses σ_u (i.e. upper) and σ_l (lower load/stress level) are related to the tensile strength f_{ct} under flexural or centric loading; n is the intended number of load cycles at each load level.

The average *flexural strength* based on the results gained from eight static tests was $f_{ct} = 37.90$ MPa. During the flexural fatigue tests, the frequency of cyclic harmonic load was 25 Hz. The average *tensile strength* based on results of static uniaxial tensile tests, was $f_{ct} = 14.90$ MPa [17]. During the axial tensile fatigue tests, the frequency of the applied cyclic harmonic load was 10 Hz.

Table 2 Cyclic testing schemes applied in tensile and flexural tests were mainly performed with macro samples (varied loading, sequence effects)

Load type	Load level 1			Load level 2			Load level 3		
	$\frac{\sigma_u}{f_{ct}}$	$\frac{\sigma_l}{f_{ct}}$	$\frac{n}{10^6}$	$\frac{\sigma_u}{f_{ct}}$	$\frac{\sigma_l}{f_{ct}}$	$\frac{n}{10^6}$	$\frac{\sigma_u}{f_{ct}}$	$\frac{\sigma_l}{f_{ct}}$	$\frac{n}{10^6}$
1	0.8	0.2	3	0.6	0.2	2	0.4	0.2	1
2	0.4	0.2	1	0.6	0.2	2	0.8	0.2	3
3	0.8	0.4	3	0.6	0.2	2	0.4	0.1	1
4	0.4	0.1	1	0.6	0.2	2	0.8	0.4	3

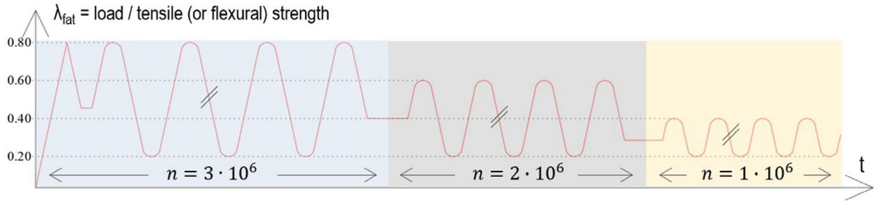

Fig. 9 Cyclic loading scheme, exemplarily shown for load type 1 (for details see Table 2)

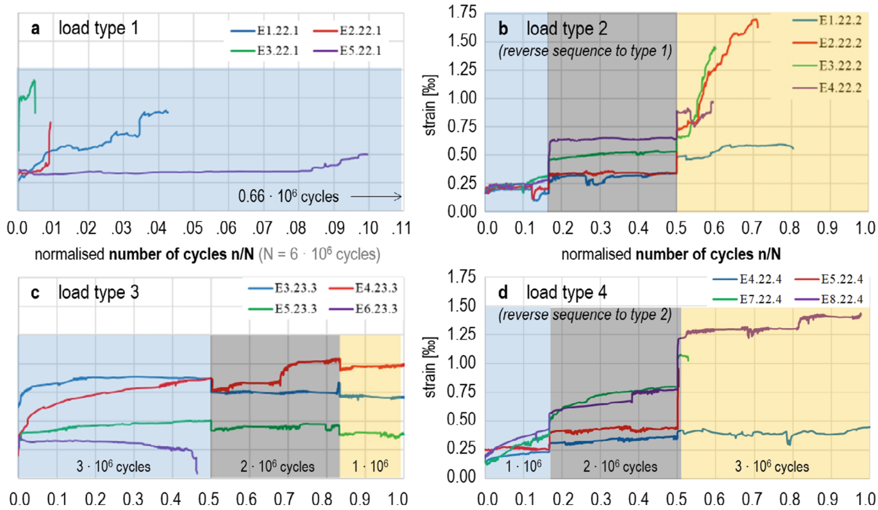

Fig. 10 Average values of strain: **a** load type 1, **b** load type 2, **c** load type 3 and **d** load type 4; the underlying maximum number of cycles N is 6 million

2.3.1 Tensile Fatigue Tests

In the (axial) tensile fatigue tests, strains were measured with four strain gauges, two of which were attached at the upper and two at the lower edge of the testing area, refer to Fig. 1a. They were orientated in the direction of the tensile stresses. Four samples were tested for every load type and the average strain for the individual specimens was determined from the measuring data of all four strain gauges. The experimental results are displayed in Fig. 10a–d.

Significant non-matching of results for different specimens can be noticed from the very beginning of the fatigue test. Results given in Fig. 10a for load type 1 show that all specimens failed during load level 1 (high initial $\sigma_u/f_{ct} = 0.8$ and high initial $\Delta\sigma = (\sigma_u - \sigma_l)/f_{ct} = 0.6$) before reaching the intended number of 3 million cycles. This indicates that the specimens were already cracked during static load increase before they were subjected to the harmonic load. Hence, the tested samples were in the range of non-linear behaviour during the entire harmonic load (fatigue test).

Results for load type 3 (high initial $\sigma_u/f_{ct} = 0.8$ but lower initial $\Delta\sigma = 0.4$) compared to type 1, Fig. 10b show a disagreement of results for different specimens from the very beginning of the fatigue test, too. Thus, cracks also appeared there during the static load increase having preceded to harmonic load. In contrast to the specimens of load type 1, the samples subjected to load type 3 withstood a significantly higher number of cycles. Three of them survived 6 million cycles, while one sample broke shortly before reaching 3 million. Figure 10b also shows a slight relaxation of strain, which may indicate closing cracks.

Results in Fig. 10c (load type 2; maximum $\Delta\sigma = 0.6$ in load level 3), and Fig. 10d (load type 4; maximum $\Delta\sigma = 0.4$ in level 3) show a good agreement for different specimens in the first million cycles (load level 1; both with moderate $\sigma_u/f_{ct} = 0.4$) indicating a global linearity of the specimens. However, a slight deviation of the results may be identified, though, which may be a consequence of the local micro-nonlinearity of the specimens. This minor deviation is a little more emphasised with specimens subjected to load type 4 which indicates a more significant local micro-nonlinearity compared to specimens subjected to load type 2. After 1 million cycles and the increase of the upper load level (to $\sigma_u/f_{ct} = 0.6$ in both cases), deviation of the individual results for both load types 2 and 4 is considerably more pronounced than in the first million cycles, although not as significant as in Fig. 10a, b. This indicates global non-linearity of the specimens caused by the microcrack pattern. However, when comparing type 2 and 4, the results are generally similar up to and including load level 2, which is to be expected due to the basically identical loading (only exception: in load level 1, lower $\Delta\sigma = 0.2$ for type 2 compared to 0.3 for type 4). After 3 million cycles and an increase in the upper load level to $\sigma_u/f_{ct} = 0.8$, no correlation can be established between the results of the different specimens (due to fully developed cracks as is also the case with the specimens subjected to load type 1 and 3) and no individual sample reaches the intended maximum number of cycles of 6 million with load type 2. But this is also to be expected because $\Delta\sigma$ for load type 2 ($\Delta\sigma = 0.6$) is significantly higher than for type 4 ($\Delta\sigma = 0.4$). Finally, a comparison of load type 1 and 2 (reversed load sequence compared to type 1) shows more favourable results when starting with initially lower upper load, i.e. type 2. This effect is significantly less pronounced when comparing load types 3 and 4 (reversed sequence compared to type 3), which may also be attributed to the stress amplitude ($\Delta\sigma = 0.4$) with type 3, which is considerably lower compared with type 1 ($\Delta\sigma = 0.60$; early fatigue failure in load stage 1). In summary, it can generally be concluded that the tensile fatigue investigations with varied loading schemes certainly provide some indications of existing sequence effects, although these cannot be quantified on the basis of the available experimental data.

2.3.2 Flexural Tensile Fatigue Tests

In flexural tests, strains were captured by one strain gauge positioned on the bottom surface of the specimens (the surface opposite to the external load) at midspan and again orientated in direction of the expected principle tensile stresses. Since specimens in load types 2 and 4 broke before reaching the maximum load level or immediately upon reaching it, only two samples could be tested with the planned number of cycles. Further, specimens tested with load type 1 and 3 respectively, a significant disagreement of the results was achieved, indicating that fully formed cracks appeared during the static load increase prior to the fatigue testing. Thus, as also observed in the tensile fatigue tests, the specimens were in the non-linear range throughout the entire harmonic load. Since there were already fully formed cracks, the energy introduced by the applied external loading was dissipated on these cracks without opening microcracks and caused failure at a relatively low number of cycles. Unlike tensile tests, in flexural fatigue tests, specimens subjected to load type 3 also broke before reducing the initial upper load level to lower value.

Overall, the flexural fatigue tests showed similar trends to the tensile tests discussed in Sect. 2.3.1, and there were also slight indications of sequence effects. However, the general scatter and deviation of results were much greater and it may be concluded that the carbon short-fibre reinforced concrete (CSFRC) has a *more favourable fatigue behaviour in tension* than under flexural tensile loading.

3 Non-destructive Measuring Techniques and Combinations

This section focuses on special NDT methods and their combinations. These techniques were used in addition to load cells, deformation/strain sensors (e.g. surface-mounted transducers, strain gauges or fibre-optic quasi-continuous sensors) in order to derive new findings on the damage behaviour and local/global damage development inside the test specimens. These results form an important additional basis for the mathematical-numerical modelling and simulation, addressed in Sect. 4.

3.1 Digital Image Correlation (DIC)

The camera-based DIC measuring technique is a very versatile method to acquire detailed information on the deformation and resulting strains on the surface of structural members. In the present project, DIC was utilised in static and dynamic tests as well as with all types of specimens, particularly with micro and macro samples. In the following, some results gained from micro/macro samples and different loading schemes are exemplarily presented; for more detailed information and a broader range of measurement results please refer to publications resulting from the present research project, e.g. [4, 8, 9, 12, 14–16, 18–20].

Regarding *micro tensile specimens* the ARAMIS 4M DIC system (GOM GmbH) was used in-situ to continuously record surface deformation/strain of the specimen with high resolution. In doing so, two CCD cameras were employed to capture the strain on the specimen surface, to which a stochastic pattern was applied. This so-called speckle pattern is customised to the specific requirements and also allows for 3D measurements that can reduce errors caused by uneven surfaces. An initial image is taken as reference before starting a test, with no force being applied [21, 22].

A sampling rate of 2 Hz was considered appropriate for capturing sufficient images during the test, while avoiding overwhelming the measurement system with storable data. Furthermore, the ARAMIS system was synchronised with the universal testing machine (Zwick Roell) to initiate recording at an initial force of 20 N, thereby establishing a direct correlation of DIC and the force and displacement signals. DIC data was analysed by using GOM Correlate Professional 2020, enabling deformation/ strain evaluation in all directions through the described methodology.

Figure 11a illustrates the force and deformation in the tensile direction relative to the cumulative number of captured images. As the data was continuously recorded at 2 Hz, the x-axis can be interpreted as time. The blue lines marked with asterisks in diagram correspond to the deformation states in Fig. 11b, where Fig. 11c represents the image of the right CCD camera after final failure.

Initially, it becomes evident that a linear-elastic region is departed around image number 535. Subsequently, the strain hardening behaviour of the CSFRC specimen becomes apparent through an increasing number of developing microcracks. These cracks mostly occur abruptly, as indicated by both an immediate drop in force and a sudden increase in deformation (also see multiscale modelling, Sect. 4). Hereby, the material's capacity for energy absorption increases by a multitude, compared to unreinforced references (see e.g. Figure 3). Microcrack formation occurs until the stress exceeds the strength of the composite material. The resulting macro crack leading to final failure was usually found in a previously undamaged region, suggesting a strong fibre-matrix interface.

In addition, DIC measurement was also used both with statically and dynamically loaded *macro tensile (and bending) specimens* to confirm and complement the results obtained from conventional strain gauges. Exemplarily, Fig. 12 shows DIC results for a dog-bone shaped specimen under cyclic varying tensile forces (loading type 3; please refer to Sect. 2.3); all DIC measurements were performed using a Stemmer camera (type Dalsa Genie Nano-M4040).

In Fig. 12a, fully formed cracks can be seen in the specimen before applying the harmonic load. The state of cracks following 3 million cycles is given in Fig. 12b. By comparing Fig. 12b with a, both new cracks opening can be noticed, but also relaxation of existing cracks, i.e. the new cracks are opened, while the width of existing cracks is reduced. After reducing the upper load level in accordance with loading type 3 (maximum cyclic load at the beginning) a further relaxation or even closure of existing cracks can be noticed, see Fig. 12c, d. These DIC results correspond very well with those obtained from conventional strain gauges.

In addition to uniaxial tensile loading, the results of cyclic 3-point *bending tests* on *macro samples* are presented below. To this end, Fig. 13 exemplarily depicts the temporal development of strain and cracking for the one bending specimen subjected to the varying cyclic loading type 4 (refer to Sect. 2.3). A strain state being able to

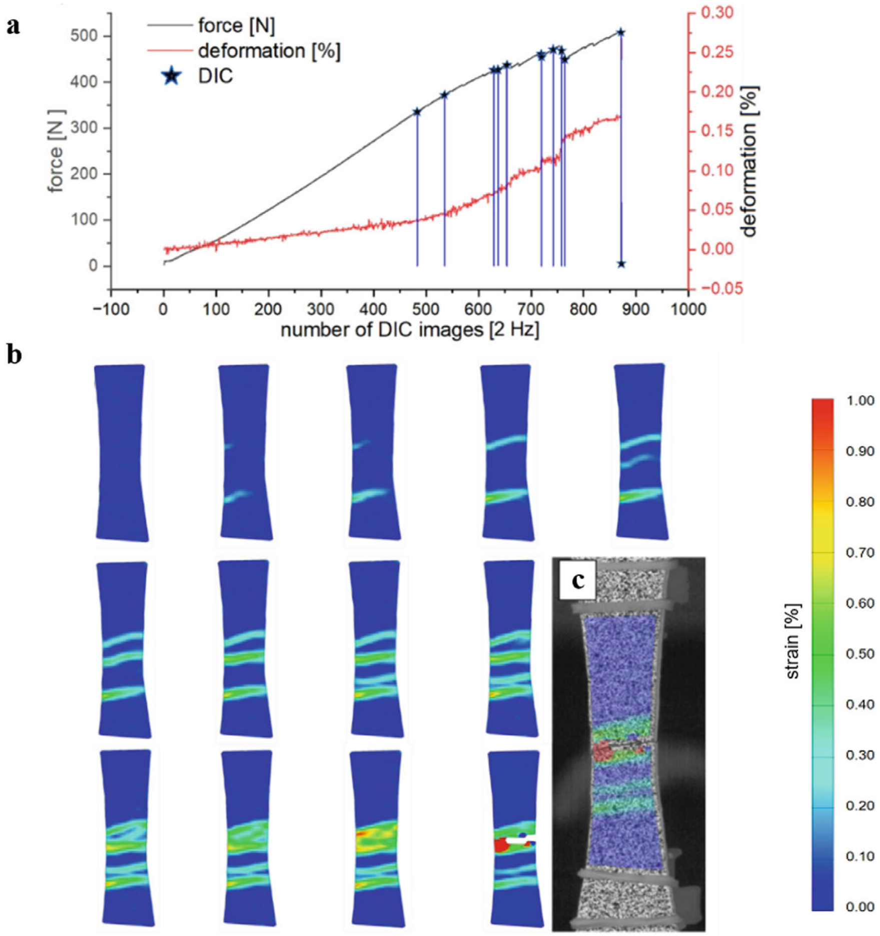

Fig. 11 Force–time–deformation diagram (**a**) recorded with ARAMIS 4M DIC, asterisks represent pictures (**b**) (no. of acquired images: 483–535–629–637–654–719–720–742–758–764–872), **c** final failure

cause appearance of microcracks can be seen after some 400,000 cycles (Fig. 13a), whereas no fully developed crack may be identified at this stage of the loading regime. Upon increasing the upper load level to 60% of the flexural tensile strength, see Fig. 13b, c, a merging of microcracks into fully formed cracks becomes apparent. When the upper load level reaches the maximal value (i.e. 80% of the flexural tensile strength), further widening of existing cracks and opening of new cracks occurs, see Fig. 13d. After utilising energy dissipation capacity of the cracking pattern developed (micro and fully formed cracks), the specimen breaks. Obviously, these results confirm those obtained from the strain gauges.

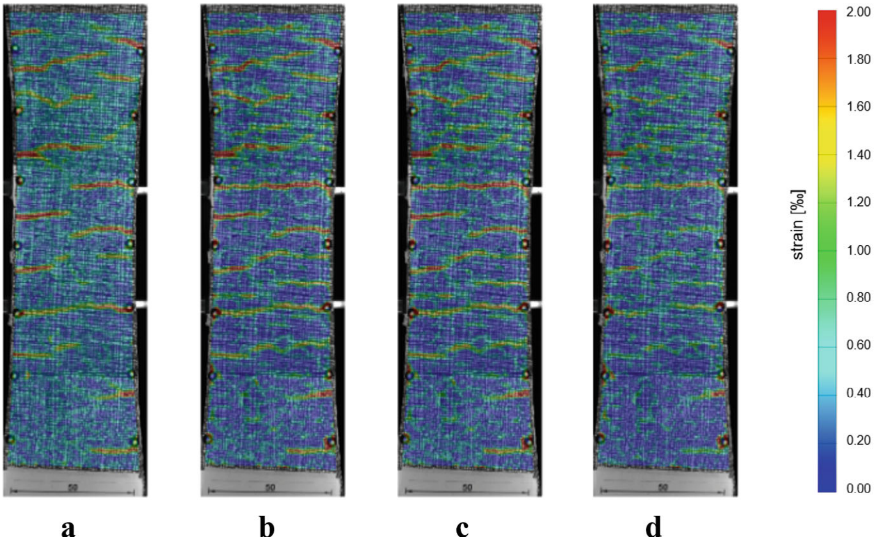

Fig. 12 DIC images for the load type 3 (refer to Fig. 9): **a** before start of harmonic load, **b** after 3 million cycles, **c** after 5 million cycles, **d** after 6 million cycles (i.e. immediately before failure)

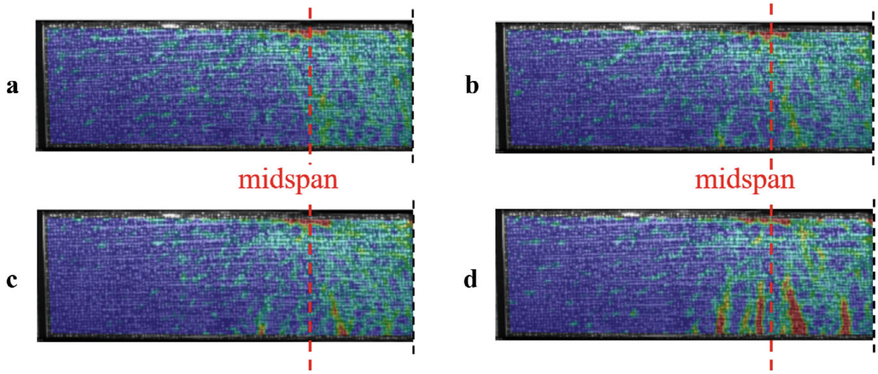

Fig. 13 DIC results for load type 4 (also refer to Table 2): **a** after 400,000 cycles, **b** after 410,000 cycles, **c** after 1 million cycles, **d** just before failure; strain scale, see Fig. 12

3.2 Electrical Measurements

In order to detect damage during load cycles, up to 17 electrodes were attached to the *macro specimens* (Fig. 14) to detect changes in voltage at several positions on the specimen's surface. The main objective was to investigate whether changes in voltage (induced e.g. by fibre pull-out or fibre breakage) can be used to detect damage propagation sooner as compared to other measurement methods. In the described uniaxial tension test with monotonic load cycles the individual electrodes are arranged on three edges of the sample with a vertical distance of 25 mm to each other. A voltage of 10 V (DC current) is supplied via a reference resistor of 10 kΩ to the electrode U_0. In [19] it is described that this measuring technique has a high resolution and fits very well to fatigue tests as single load cycles can be detected. Further information to the setup can be found within the cited paper.

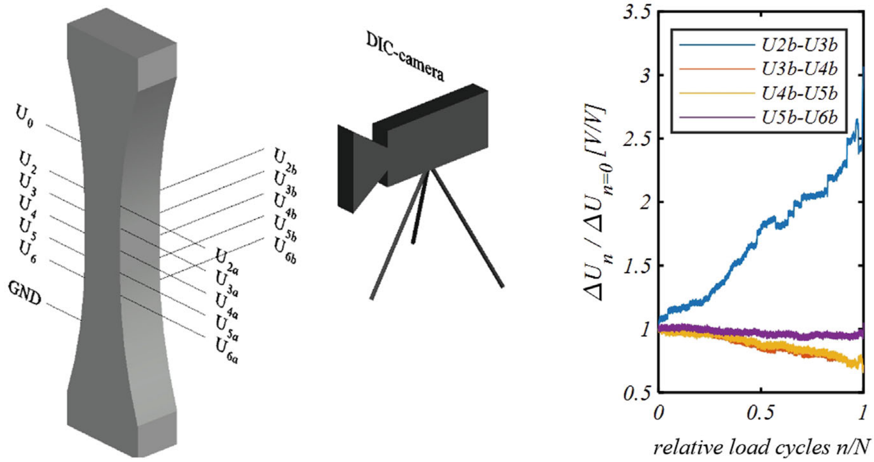

Fig. 14 Schematic sketch of measurement layout during fatigue test showing the location of the electrodes and the position of the DIC camera—current driving from U_0 to GND; relative voltage evolution with clearly revealing areas of damage progression (N = 409,063 cycles)

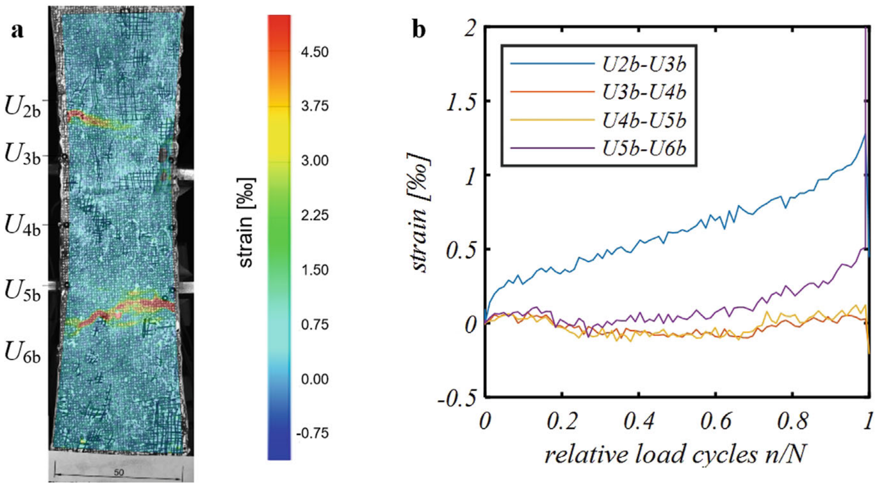

Fig. 15 DIC strain measurement (**a**) (sample surface; electrodes U_{2b}-U_{6b} attached on left side); the diagram **b** displays strain between the electrodes, which shows very similar results as in Fig. 14

As current is applied only to one individual electrode, all voltage measurements at the other electrodes depend on changes in voltage of this specific electrode. This is because changes in overall resistance of the specimen lead to a different relationship between the specimen's resistance and the constant reference resistor and therefore the applied voltage divides differently. To cancel out this effect, the change of two adjoined electrodes is examined. In order to improve further, the change in voltage between two adjacent electrodes is related to their primary voltage drop in the first load cycle as shown in the diagram in Fig. 15. This can be described with Eq. (1), where i denotes the electrode number and n the load cycle.

$$\frac{\Delta U_{\mathrm{n}}}{\Delta U_{\mathrm{n}=0}} = \frac{U_{\mathrm{i,n}} - U_{\mathrm{i+1,n}}}{U_{\mathrm{i,n=0}} - U_{\mathrm{i+1,n=0}}} \tag{1}$$

Comparing this result with digital image correlation (DIC) proves very well the reliability of the electrical conductivity measurement. The electrodes were attached to the left side as shown in Fig. 15. The image was taken at a relative load cycle of 0.99 (i.e. shortly before collapse). In this stage there are many microcracks all over the specimen's surface visible in a light blue colour. Two major cracks (though with a very small crack opening of some 40 μm) arose during a fatigue test with a high tensile strain marked in red. The crack in the lower area between electrodes $U_{5\mathrm{b}}$ and $U_{6\mathrm{b}}$ is not totally proceeding to the left edge, while the one in the upper area (at electrodes $U_{2\mathrm{b}}$ and $U_{3\mathrm{b}}$) seems to originate from there. This perception matches the curve progression in Fig. 14. Evaluation $U_{3\mathrm{b}}$-$U_{4\mathrm{b}}$ and $U_{4\mathrm{b}}$-$U_{5\mathrm{b}}$ behave simultaneously while the other two detect some change in electrical conductivity. As the upper crack is very close to the electrodes, the current is forced to find a way around the crack and the measured voltage difference increases vastly. As the lower crack barely reaches the electrodes on the specimen's left edge, the measurement of sensor $U_{5\mathrm{b}}$-$U_{6\mathrm{b}}$ is hardly affected by the crack formation. Compared to the diagram given in Fig. 15, the strain evolution matches the resistivity revolution very well.

To improve both testing and localisation, additional investigations are necessary. Connecting electrodes on all four sides of the specimen or with a fine-meshed sensor grid distributed over the surface can help to detect fatigue damage more accurately. Also applying the voltage during fatigue tests to different electrodes for only a short time while measuring the voltage at all other electrodes in a cyclic/repeating manner might reveal internal damage. This technique is called electrical resistivity tomography (ERT) and has already been used in geophysical surveys for decades.

3.3 Acoustic Emission (AE) and Laser Doppler Vibrometry (LDV)

The AE measuring method is based on elastic wave propagation rediated from internal cracking and described in the literature, e.g. [23–25]. Since AE can be applied under operating conditions without stopping machines and equipment, it is a highly efficient tool for remote control. Understanding the damage process can be significantly improved by signal-based processing techniques that allow the extraction of the maximum amount of information recorded in the entire AE signal waveforms, refer to e.g. [26]. AE is beneficial in fatigue testing of high-performance materials, e.g. [14, 27, 28]. On the one hand, these materials have excellent durability and can resist destruction for long periods of time, thereby providing enough time to detect damage and to monitor its dynamics. On the other hand, the damage accumulation in heterogeneous materials is accompanied by a more active and complicated AE response, which is influenced by the properties of the composite constituents, their volume fractions, and spatial distribution [9, 29–31]. Dynamic load tests show that the fatigue process in fibre-reinforced material generally occurs in several stages, differing in AE signal characteristics. There, the first elastic deformation is followed by the so-called strain-hardening stage [32, 33]. It is characterised by the occurrence and growth of multiple cracks within the matrix, which cannot spread far due to the presence of fibres. The carbon short-fibres, which are stronger than the matrix, take on further stress and maintain the material's resistance in tension (fibres bridge the cracks) until it exceeds the maximum bonding capacity (anchorage of the fibres on both sides of the cracks) or the ultimate tensile strength of the fibres (fibre failure). The cracks' distribution over quite a large area is a typical damage pattern developing in high-performance concrete—in contrast to standard concrete, being characterised by localised damage, e.g. [15]. Many studies accompanied by AE analysis show that low-energy and -frequency AE events are associated with matrix micro-cracking, while high-amplitude and -frequency signals are caused by fibre breakage and may be predictors of fatigue failure, see e.g. [34, 35]. The most promising strategy for analysing internal damage mechanisms is data clustering, where AE signals are combined into groups with identical characteristics (frequency, amplitude, duration, etc.) corresponding to a specific damage mechanism, see e.g. [28, 36–38].

3.3.1 Static Tensile Tests Equipped with AE Sensors

In this study, both AE and DIC were applied jointly to better characterise the damage progress in CSFRC. In the first phase, the material's damage behaviour was studied in tensile tests subjected to monotonous fatigue loading. To ensure stability of the data acquisition, four small passive piezoelectric AE sensors were glued to the specimen (with 1 vol.% CSF) and then connected to the acquisition system.

The root-mean-square value of a raw acoustic signal RMS_{AE} was used to represent the intensity of the AE because it is directly proportional to the strength of the acoustic signal and thus, its energy. Analysis of the AE activity is based on the interpretation of one of the most relevant parameters of the AE signal, the cumulative number of acoustic emission events. One-dimensional localisation was performed using MATLAB©. AE signals were localised in linear geometry based on differences in signal arrival time between the different sensors. Onset times of AE signals were

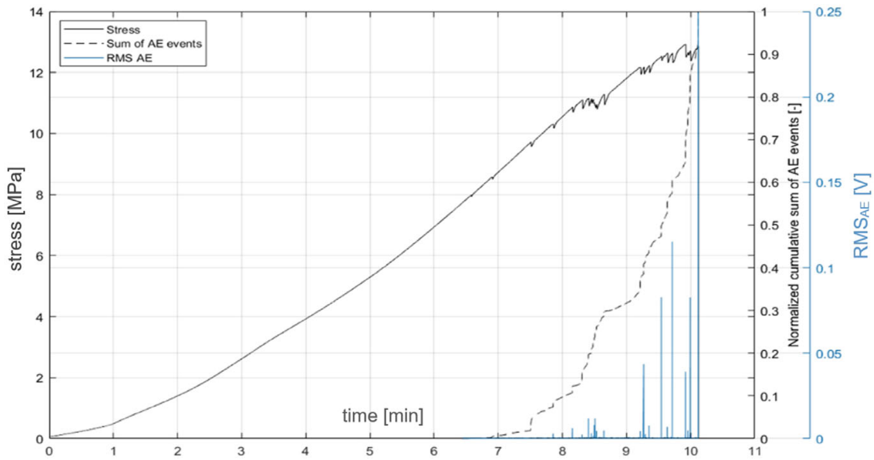

Fig. 16 Characteristics of AE: normalized cumulative number of AE events (in black, dashed curve), RMS_{AE} (in blue), and a mechanical parameter, stress (in black), as a function of time

picked automatically using an autoregressive algorithm as time points where Akaike Information Criterion (AIC) values were minimal.

Figure 16 shows the representative response of acoustic emission signals, normalised cumulative number of AE events, RMS_{AE} and a mechanical parameter, stress (in black), plotted as a function of time for a meso tensile specimen with 1 vol.% of carbon fibres. As the graph indicated, there is no acoustic activity in the first half of the test regime. After about 6.5 min, first AE events appear, but AE activity remains low for some time (up to 80% of the test duration), suggesting that the sample reached the strain-hardening phase. The appearance of low-intensity acoustic signals is associated with the formation of microcracks in the concrete matrix, which stabilise the specimen material and allow to resist load more effectively.

Active acoustic emission mainly accompanies the last 20% of the loading time. During this period, most of the acoustic events occurred, causing a dramatic increase in AE energy with the highest peaks shortly before specimen failure (after 90% of the test time). Thus, the response of the specimen to loading is characterised by the appearance of acoustic phenomena in the second half of the test. A sharp increase in AE intensity at the last stage, manifested by high RMS_{AE} amplitudes, indicates further rapid formation of microcracks and an accelerated crack growth.

Figure 17 shows the sample after failure and distribution of localised AE events. The cause of the failure was a perpendicular fracture. For this specimen, sources of AE events are concentrated within some 3 mm, with the maximum number of events generated close to the primary fracture. The spatial distribution of the AE events approximately corresponds to the width of the damage zone. The scatter plot, see Fig. 17a, shows the temporal localisation of the acoustic emission events. It is noticeable that the first events occur after 6.5 min and correspond to the position of the main fracture. As the test time progresses, the number of events increases at the

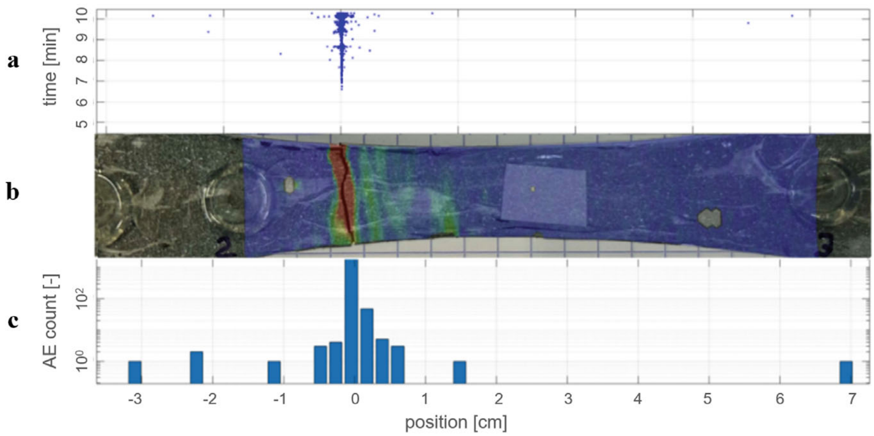

Fig. 17 Scatter plot **a** illustrates temporal distribution of AE events; image **b** displays crack pattern visible by overlaying the picture of the specimen with the recorded DIC data; histogram **c** showing the spatial distribution of the AE events along the specimen

location of the primary fracture and within a radius of some 5 mm right of it, where additional cracks begin to form. When reaching the final time (approximately after 10.2 min), the main fracture leads to the failure of the whole sample.

3.3.2 Static Flexural Test with AE and Laser Doppler Vibrometer

During this 3-point bending test, the same measurement setup for the AE recording was used (see Fig. 18), as mentioned above in Sect. 3.3.1. The detailed analysis of the AE parameters for the flexural static test can be found [15].

In order to detect high-frequency signals resulting from the main characteristic damage mechanisms of the fibre-reinforced cementitious material (in particular fibre pull-out and/or fibre breakage), it was decided to supplement AE measurements with LDV, which makes it possible to obtain data in frequency rages of more than 1 MHz. Hereby, a LDV system from POLYTEC with OFV-505 single-point measuring head and OFV-5000 controller, was employed. Further, a DD-300 (30 kHz–24 MHz frequency range) with measurement range of approximately $\pm$ 50 nm/V and an additional output in the auxiliary field was used as a displacement decoder.

Figure 19 shows a graph of the cumulative sum of AE events combined with a stress–time curve, where it is possible to distinguish two different stages that differ in AE activity and mechanical response of the specimen. At the first stage (0–1.5 min), the linear shape of the stress curve and the absence of acoustic events indicate that the material retains the ability to deform elastically under an applied load. In the second stage, upon appearance of the first AE signals, moderate activity was recorded until approximately 3.5 min. Then, the AE activity begins to increase and reaches a maximum shortly before destruction of the specimen. The signal selected for wavelet

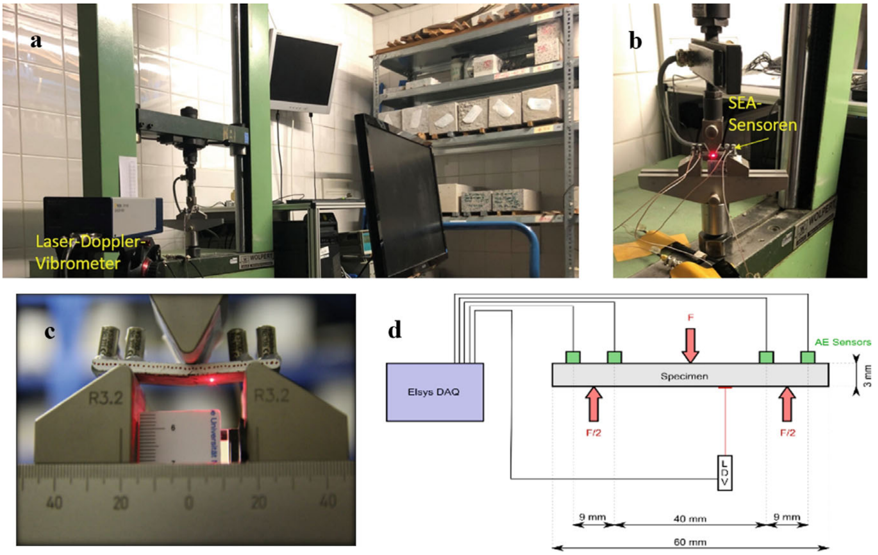

Fig. 18 Experimental setup for static 3-point test with AE and LDV (**a**, **b**); **c** loaded specimen with four sensors glued onto it; **d** specimen with dimensions and AE sensor arrangement (sketch)

analysis was recorded at a point of time of about 20% before the specimen's failure. At this time, the curve of the cumulative sum of AE events becomes steeper, reflecting the rapid progression of damage with potential fibre involvement.

In order to determine the underlying damage mechanisms, the signal's frequency components were analysed using the analytic Morlet wavelet transform, which decomposes the signal into a series of small waves localised in time. This offers advantages over other time–frequency analysis methods, such as the Fourier transform, which implies that the frequencies are maintained throughout the entire signal. The same signal recorded in the last quarter of the measurement time was selected for analysis (see Fig. 19). A wavelet transform was performed on the AE and LDV signals, see Fig. 20a, b. The results of an analytic Morlet wavelet transform of these signals are shown in Fig. 20c, d. Thus, it is possible to identify the contribution of the frequencies 100, 280 and 800 kHz in the frequency spectrum. Hereby, the AE signal showed lower frequencies (280 and 100 kHz), while the vibrometer recorded the signal with higher frequency of 800 kHz. Signals of different frequencies can be attributed to different destructive and damaging processes, which occur simultaneously and suggest a complex failure mechanism involving damage to both matrix and fibre phases. The lower frequencies of 100 kHz can be associated with matrix cracking, while the higher frequencies can be attributed to pull-out of fibres and fibre breakage. More information on this topic can be found e.g. in [8].

The present investigations confirm that laser Doppler vibrometry can be used in addition to acoustic emission to draw conclusions on complex fracture mechanisms.

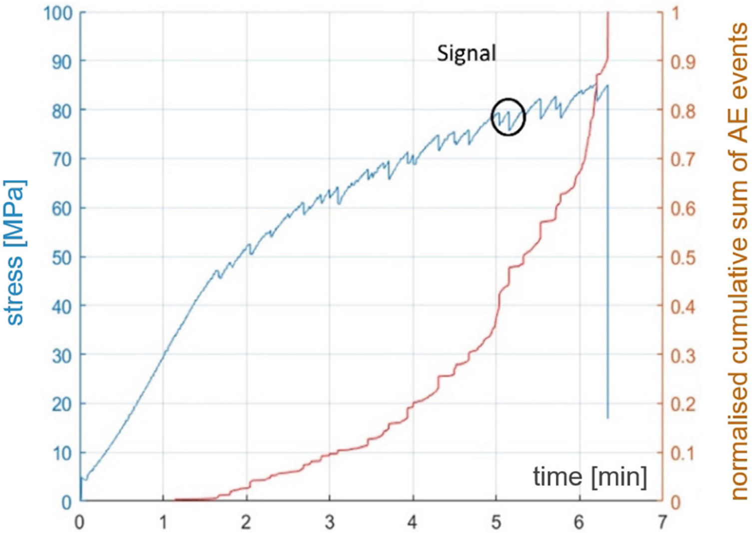

Fig. 19 Recorded parameters for one sample during 3-point bending test (normalised cumulative no. of AE events (in red) and stress curve (in blue) as a function of time) with the approximate position of the selected signal for further wavelet transform

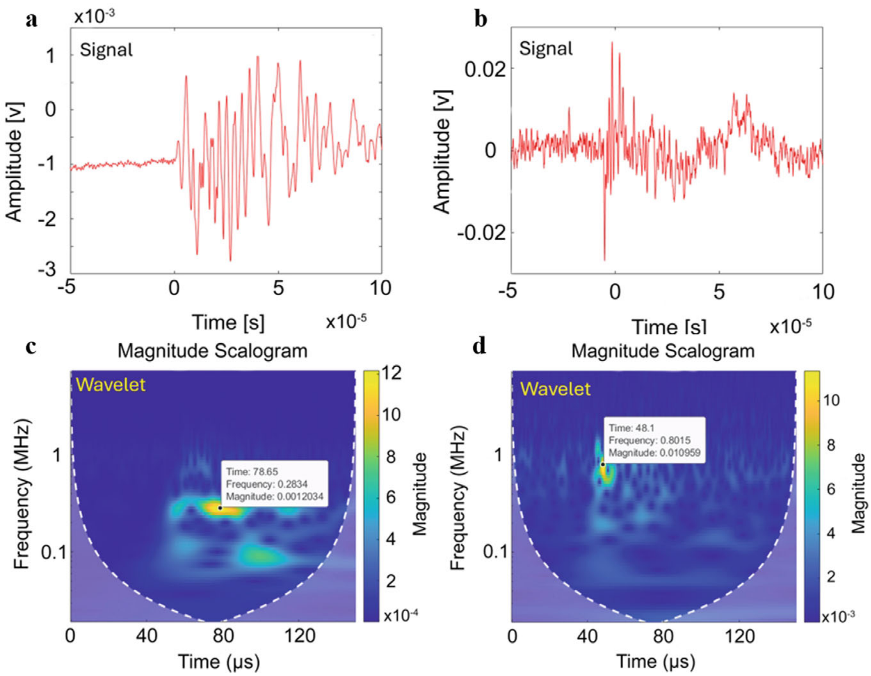

Fig. 20 **a** AE signal used in wavelet transform; **b** LDV signal used in wavelet transform; **c** analytic Morlet wavelet transform of AE signal **a**; **d** analytic Morlet wavelet transform of LDV signal **b**

3.3.3 Dynamic Flexural Test Equipped with AE Sensors

Since most engineering structures experience loads varying over time, an experiment with dynamic loading makes it possible to identify the characteristics of the fatigue behaviour of a material under conditions close to real ones.

AE measurements were carried out using four small-sized passive piezoelectric sensors AE VS700-D (150–800 kHz), placed at the edges of a micro bending beam specimen and coupled with hot glue. The tested sample (with 1 vol.% of fibres) had dimensions of 50 × 12 × 1.5 mm. Measurements were carried out with a DMA machine with a lower force of 4.3 N, an upper force of 13.2 N, and a frequency of 10 Hz. The data acquisition system "Elsys" recorded AE signals at a sampling rate of 20 MHz and converted them to digital form. The experimental setup with the DMA can also be seen in Fig. 7 (left), the arrangement of the AE sensors is in analogy to Fig. 18d. The cumulative sum of AE events/activity was investigated through time domain analysis of the AE signal characteristics. Further, the emission intensity was analysed by estimating the root mean square value of the original RMS_{AE} signal which is proportional to the strength and the energy of the AE signal.

Figure 21 shows the characteristics of the AE signal, the RMS_{AE}, the normalised cumulative sum of AE events and a mechanical parameter, the strain ratio, plotted against the cycle ratio. Based on the AE analysis, four periods of different AE activity which correlate with the specimen's mechanical behaviour can be observed. In the initial period of the test, i.e. 0–0.07 of the total number of cycles, the acoustic emission activity is low. Only sporadic events with low energy levels are recorded during this time. In the second period (0.07–0.3 of the cycles), the number of AE events increases sharply. The slope of the cumulative curve of AE events becomes almost vertical, suggesting that the AE event rate accelerates rapidly. This coincides with a noticeable increase in the AE energy. The intensity of the AE signal began to fluctuate more, and the first signals with higher energy appeared. During the further loading cycles (0.3–0.8 of cycles), the acoustic activity decreases and remains very low for a long time, as being indicated by the nearly horizontal cumulative curve. During this period, the strain ratio did not noticeably increase, constantly remaining within 0.95–0.96 of its maximum values. At approximately 0.78 of the load time, high-energy signals appear on the RMS_{AE} graph. This clearly correlates with the onset of a rapid increase in strain. During the last 20% of the loading time, AE signals again become more frequent and intense, with the highest energy signal occurring at the moment of specimen destruction.

Thus, after the peak of acoustic emission in the early cycles, there is a relatively quiet period with minimal AE activity, which continues throughout most time of the test. The increase in the number of AE events and the appearance of high AE energy peaks in the last 20% of the test time can be considered a sign of impending material failure. Hence, analysis of the characteristics of the AE signal makes it possible to distinguish the stages of damage accumulation in the material, namely the formation of microcracks in early loading cycles, a further state of equilibrium, indicating the ability of the material to resist deformation, and, ultimately, in the final part of the test, accelerated damage with further crack formation and their (unstable) growth.

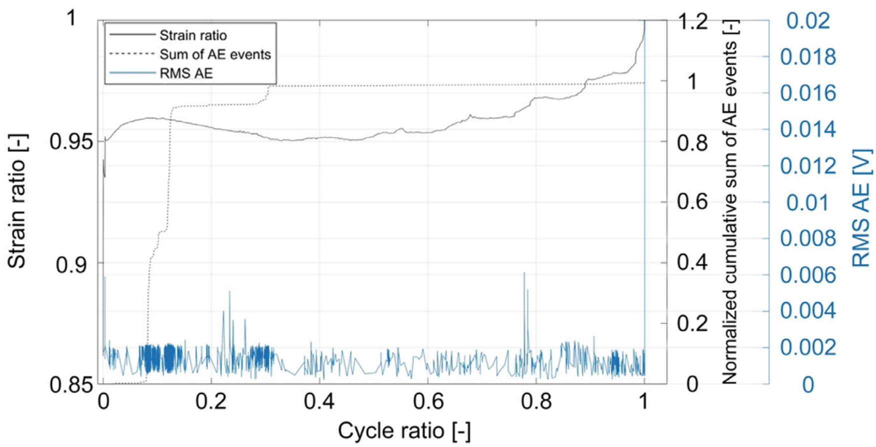

Fig. 21 AE signal characteristics, RMS_{AE} (in blue), cumulative sum of AE events (black dashed curve) and strain curve (in black) for micro beam specimen, plotted against the cycle ratio

3.4 X-Ray Computed Tomography (CT)

All X-ray images were taken with a Phoenix nanotom 180 m scanner (GE Sensing & Inspection Technologies GmbH). To correlate the mechanical behaviour with the fibre alignment present within the CSFRC samples, the distribution of the alignment angles was investigated using X-ray CT [32]. Figure 22a shows the distribution of in-plane angles with standard deviation shaded in red. Figure 22b presents a scan excerpt, showing the segmented fibres with the distribution being highlighted in blue. For the purpose of this publication, fibres being aligned with the principle tensile stresses are designated as having an alignment angle of 0°.

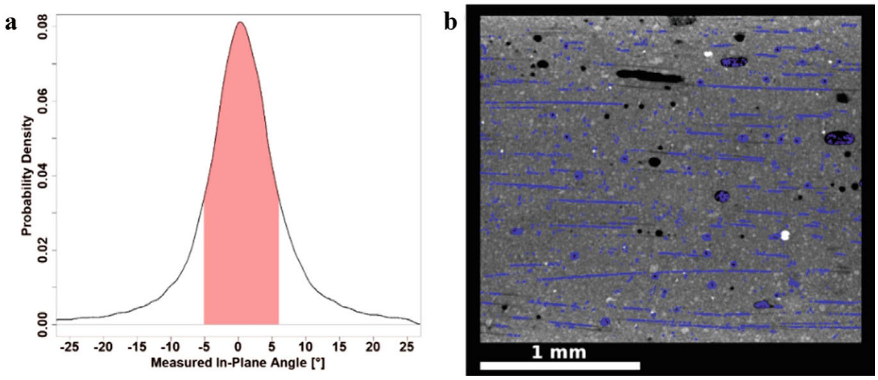

Fig. 22 Fibre alignment in a sample measured with X-ray CT: **a** distribution of in-plane fibre angles (red area: standard deviation); **b** tomographic scan (segmented fibre material in blue)

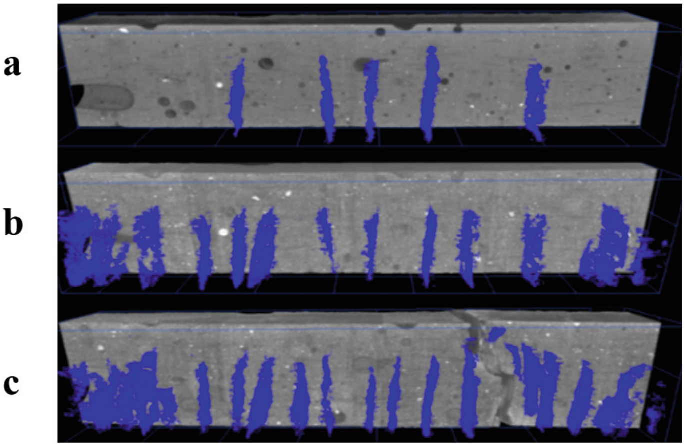

Fig. 23 Segmented cracking patterns of an extruded micro beam specimen during fatigue loading. Numbered intervals correspond to points annotated in Fig. 8. (1) Crack pattern after 0.2% of runtime of the fatigue experiment; (2) cracking after 24% of runtime, and (3) crack pattern after failure. Adapted from [16], with modifications

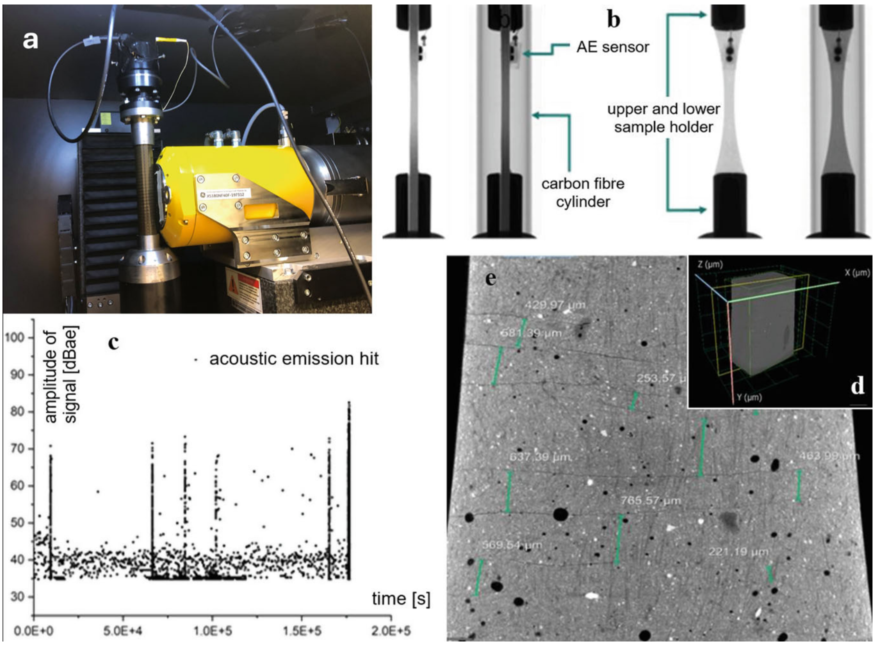

Fig. 24 **a** In-situ CT loading setup (micro tensile samples); **b** X-ray CT scan of specimen with 90° and 0° in different greyscales, right ones showing sample chamber; **c** AE hits during tensile test with peaks (formation of microcracks); **d** reconstruction of 3D image where plane **e** is extracted

As can be seen from Fig. 22a, the in-plane alignment scatters around the desired angle of 0°. Further, the standard deviation shows, that 68% of the fibres are aligned within ± 5° of the direction of the expected tensile force. Previous research suggests, that as long as the alignment reinforcement does not deviate by more than 10° from the direction of the acting stresses, a very strong composite material can be created [14]. The resulting potency of the aligned reinforcement can be seen in Fig. 3a, showing stress–strain diagrams of micro flexural beams reinforced with up to 3 vol.% of fibres, in comparison with an unreinforced specimen for reference.

The cracking patterns visualised in Fig. 24 (corresponding measurement data gained from segmenting the cracks can also be seen in Table 3) support the conclusion drawn from the assessment of SM and LM in Fig. 8. The scan corresponds to a runtime of 0.2% or just a few hundred load cycles. Cross-referencing with Fig. 8 reveals that this is during the first loading period where the micro beam exhibits a drastic decrease in both moduli and a lot of the initial damage seems to occur. At this point, the test beam shows five segmentable cracks with a relatively wide spacing of 933 µm in average. Point (2) was taken during the steady-state period at a cycle ratio of 24.4%, after the initial damage has formed. The crack number triples to 15 and consequently, crack spacing becomes a lot tighter (550 µm). As expected, the formation of new cracks is mostly confined to the earlier stages of fatigue. After failure (and thus at a cycle ratio of 100%) at point (3), a number of 23 segmentable cracks can be identified, as well as a large critical crack causing final failure. Crack spacing also only decreased relatively little to around 400 µm.

As the former experiments describe ex-situ X-ray investigations, it was also possible to do in-situ tests. An X-ray CT in-situ tensile test was carried out using a load stage that was developed in-house by the MRM Institute at UNA and integrated in the nanotom [39]. The experimental setup is illustrated in Fig. 24a. The loading device was attached to a turntable positioned in the CT, such that the specimen inside a carbon fibre reinforced polymer tube was directly in front of the X-ray source. Figure 24b shows sample holders, where the right pictures have a higher greyscale to show the experimental setup within the sample chamber. The dimensions of the chamber also allowed for attaching an AE sensor to the sample, enabling continuous monitoring. An HD2WD sensor (Mistras) was connected to the sample surface with Korasilon paste aided by 3D-printed sample holders, and connected to a differential preamplifier (Mistras) [40]. Before onset of loading, a reference CT scan was performed. After starting the experiment, the force increase was interrupted after many AE hits were recorded and another CT scan was taken. The very last AE

Table 3 No. of cracks and crack spacing extracted from CT scan given in Fig. 23

Cycle ratio (%)	Mean crack distance (µm)	No. of segmented cracks
0.2	933 (± 359)	5
24.4	549 (± 193)	15
100.0	401 (± 161)	23

peak in Fig. 24c is the final failure. Further, Fig. 24e shows the plane taken from the 3D image (marked in yellow in Fig. 24d), which was the last scan before failure.

The average crack spacing is about 497 µm while average opening is some 7 µm but can vary from 10 to 2 µm, although latter value is close to the resolution limit, but the important difference is that the force was not reduced during the scan, which gives us strong evidence that the carbon fibres bridge microcracks and absorb stress although the matrix is already widely cracked. For more details, please refer to [18].

4 Multiscale Modelling, Simulation

The CSFRC material involves different length scales, most importantly fibres with 7 µm diameter preferably oriented in direction of the principle tensile trajectories, the fibre length of about 3 mm and the sample size of several cm. The aim is to characterise the failure behaviour of the composite material exposed to increasing tension numerically based on the experimental observations, performed with different specimens and on different scales (micro, meso, macro). By modelling and simulation, it is possible to derive a better understanding of the local load-bearing and failure mechanisms on the microscale and how these mechanisms are related to the macroscopic material properties and stages of damage. Due to the novelty of the material, the damage mechanisms involved in failure of the bulk material have not yet been determined sufficiently in detail. Accordingly, it is of fundamental interest to explore further which of the mechanisms typically occurring in fibre composites, such as debonding and anchorage failure (i.e. fibre pull-out), fibre breakage or matrix failure, are relevant for the overall behaviour of the material. Thus, different possible damage scenarios are derived and validated from the experimental results aiming to develop a general failure model. The experimental data, particularly from CT and DIC analyses of tension tests (see Sect. 3.4), deepen the understanding of relevant damage mechanisms on the microscale in the material and provide the information for developing the failure model. Here, the different involved length scales require the application of mathematical multiscale methods since direct simulation of the whole specimen including the resolution of the microstructure is not feasible. Therefore, a structure-oriented numerical multiscale model of the material is developed.

In contrast to typical FE^2 methods (see e.g. [41] or, for a recent overview, [42]), adapted methods based on periodic homogenisation on the continuum scale in conjunction with discretisation by finite elements are used to simulate the behaviour of a specimen in the experiment, where the local material law in each macroscopic point is determined by solving so-called cell problems on representative volume elements (RVE) on the fibre scale (see Fig. 25).

This derived local effective macroscopic material law is used for the simulation at the macro scale, i.e. of the entire specimen. Following this general idea, it is not only possible to simulate the undamaged material (see Sect. 4.2) but also to include different failure stages in the specimen according to the damage behaviour observed in the experiments by allowing damage to evolve in the RVEs (compare Sects. 4.2,

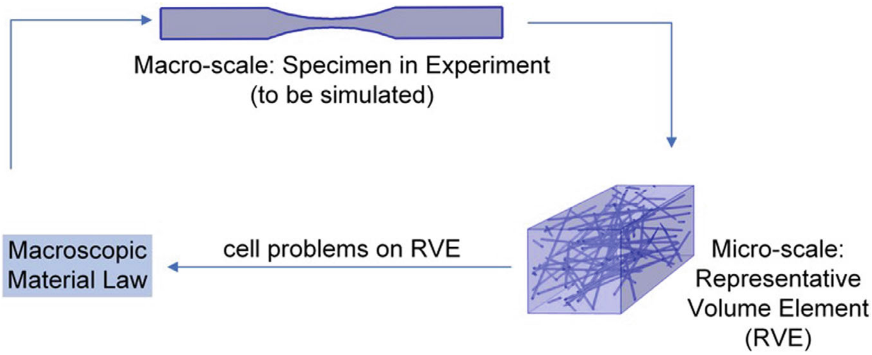

Fig. 25 Adapted homogenisation method

4.3 and Fig. 28). An essential criterion for the numerical model is its simplicity and efficiency with a sufficiently accurate representation of the relevant mechanisms. Following this guiding principle, the implementation is conducted in the sense of an experimental virtual lab, not requiring too much computational capacity and being based on the standard engineering software COMSOL Multiphysics® [43] as a basis to enable a potentially broad use. The investigations are limited to material with 1 vol.% of carbon fibres. Hereby, the small fibre diameter leads to a relatively high number of fibres, causing various problems in mesh generation the more fibres the material contains. Further, the occurring mechanisms are structurally the same but the individual effects of damage overlap with higher fibre content.

4.1 Homogenisation Method

The concept of homogenisation treats numerical issues involving composite materials where the macroscopic scale is far larger than the characteristic length of the microstructure. Resolving the whole specimen including the microstructure for simulation is numerically not feasible. Therefore, analytical techniques are used to derive an effective continuum model describing an artificial (homogenous) material with approximately the same macroscopic properties as the original problem by a rigorous limit procedure. As a result, the linear elasticity equation for the unknown displacement u is obtained as

$$-\nabla \cdot \sigma = f, \quad \left(\text{with:} \quad \sigma = A^{hom} e(u); \quad e(u) = \frac{1}{2}\left(\nabla u + (\nabla u)^T\right)\right) \tag{2}$$

with the stress tensor σ and A^{hom} representing the local effective material tensor of the artificial homogenous material while $e(u)$ is the linearized strain tensor and f is the force density (with respect to volume). The macroscopic relationship of the stress and the strain tensors described via the homogenised tensor A^{hom} can be computed by mean values of quantities determined by so called cell-problems in local representative volume elements Y (see RVE in Fig. 26 and the RVE description in Sect. 4.3.1) as follows

$$A^{hom} = \left(a_{ijkl}^{hom}\right)_{1 \leq i,j,k,l \leq 3} \tag{3}$$

with

$$a_{ijkl}^{hom}(x) = \frac{1}{|Y|} \int_Y A(x, y) e_{ij} \left(e_{kl} - e_y \left(w^{kl}\right)(x, y)\right) dy,$$

where x denotes the macroscopic spatial variable in the specimen and y is the microscopic spatial variable in the RVE Y. The corrector functions w^{kl}, $k, l \in \{1, 2, 3\}$ are unique solutions of the cell problem

$$-\nabla_y \cdot \left(A(x, \cdot)\left(e_y\left(w^{kl}\right)(x, \cdot) - e_{kl}\right)\right) = 0, \tag{4}$$

subject to periodic boundary conditions and having zero mean value, where A describes the material properties of the different phases in the RVE. For more details, please refer to e.g. [44, 45].

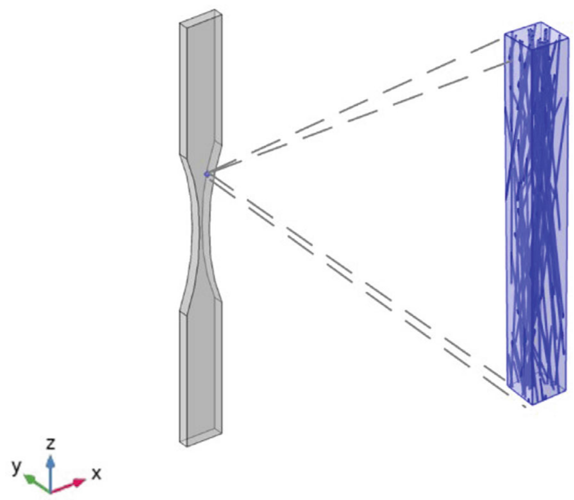

Fig. 26 Principle of homogenisation with local macroscopic undamaged RVE

4.2 Undamaged Material

A crucial aspect of models based on mathematical homogenisation approaches is the determination of RVEs which are representative for the entire material, here consisting of concrete and 1 vol.% of oriented carbon fibres. Further, the efficiency of the numerical model depends on the choice of the mesh, which is just fine enough to resolve all relevant mechanisms. Careful specification of an appropriate RVE and the optimum mesh size is therefore the starting point not only for simulation of undamaged material but also for further modelling of the damage mechanisms. Based on preliminary studies, aggregates on fibre scale and pores on fibre as well as specimen scale are neglected, meaning that the RVEs only consist of the concrete matrix and the fibres. In addition, it is assumed that the bonding between fibre and concrete matrix is perfect. The case where weaker bonding is assumed and modelled via slip-displacement conditions is investigated in [46]. The derived homogenised problem shows only marginal impact of the weaker bond on the macroscopic behaviour in the case of undamaged concrete. In [15], the authors studied the sufficient size of the RVE, which is as small as possible and still representative for the material. The fact that the fibres are small in diameter (7 μm) but long (about 3 mm) leads to long RVEs of small cross-section. With these results and from the statistical data concerning angular orientation of the fibres, a final RVE of the size 317 × 317 × 3000 μm with oriented carbon fibres was constructed (see also Fig. 27 for the RVE of the undamaged material). Further detailed convergence studies on the size of the mesh elements were conducted. In the simulations presented below, the mesh consists of 195,105 tetrahedral mesh elements resulting in 834,717 degrees of freedom (quadratic Lagrange elements). By using this RVE, the macroscopic material law for the undamaged material is derived according to Sect. 4.1, which is relevant for the first phase of the tensile tests (see Sect. 3.3.1). Based on these results and the RVE for the undamaged material, further adaptations are made for considering damage mechanisms relevant in stage II of the degradation process.

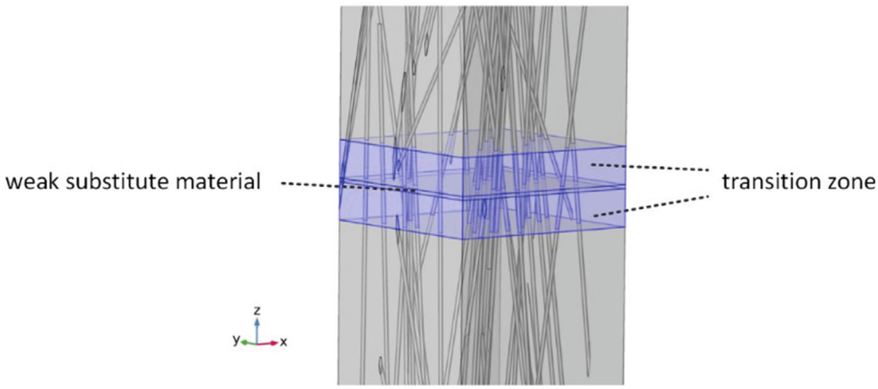

Fig. 27 Damage model via weak substitute material and transition zone

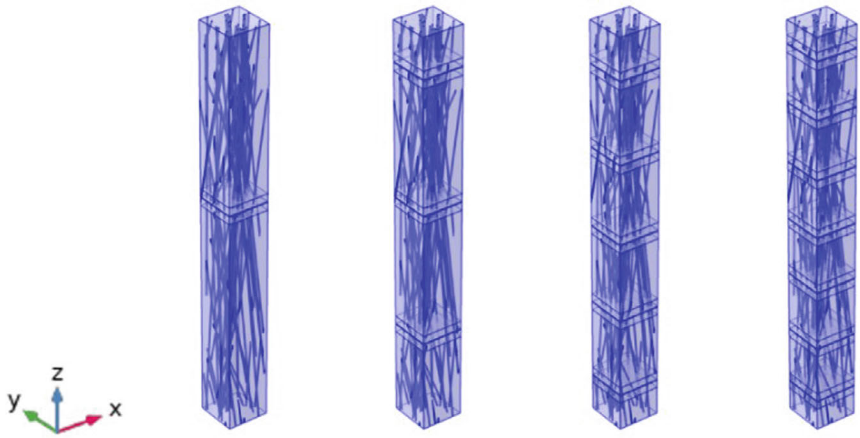

Fig. 28 Different stages of RVE damage with 1, 3, 5 and 7 cracks (left to right)

4.3 Modelling of Damage Behaviour and Relevant Mechanisms

The main goal is to understand the principles leading to fatigue and failure of the material and to implement a model which reproduces the relevant mechanisms. The experimental results serve as input for the numerical model. The comparison of the stress–strain diagram (see Fig. 11a) and DIC images evaluated at the corresponding points in time (e.g. Figure 11b) show a direct correspondence of sudden damage in the material and the drops in measured stress. Furthermore, it is seen from these experimental results of samples with fibre content of 1 vol.% that, between these events, the material behaviour can be considered as piecewise linear. Similarly, in experiments with samples with higher fibre content, only higher crack density is observed until final failure, where each cracking event is still associated with a drop of stress, leading to a smoother appearance of the measured stress–strain diagram. The DIC results further show regions with different strain, which is associated with different amounts of material damage, i.e. crack density. Comparing the DIC and the CT images (see Figs. 11 and 24), it can be seen that, during the tensile tests with the small specimen, complete crack propagation through the matrix of the component takes place without inducing further crack opening in fibre direction or complete failure of the component which allows for further damage in form of cracks at other positions. Also, the fact that, as stated in [40], the initial crack does not necessarily develop as fatal crack leads to the conclusion that the oriented fibres firstly bridge the progressing cracks in the concrete matrix. This substantiates the hypothesis that following onset of cracking little to no fibre-related damage, e.g. fibre pull-out or breakage, occurs in the cracked area until final failure and the fibres bridge the material. It is deduced that the material-typical strain-hardening-like behaviour [15], which is typically observed in samples with a significant volume content of oriented fibres, results from superposition of multiple events causing stress drops.

4.3.1 Modelling

From these results/observations, the following assumptions are extracted: the relevant 'failure' mechanism on microscale level is the sudden cracking of the concrete matrix without fibre-related damage. Crack propagation on RVE scale is instantaneous during the considered time scales. Thus, on macro scale, locally only either un-damaged RVEs or RVEs with cracks in the matrix perpendicular to the fibre orientation through the whole RVE are considered. The number of cracks per RVE varies in the experiments according to the length of the respective RVE, from 1 to 7 cracks.

The macroscopic damage and successive development of damaged zones in the specimen can thus be modelled locally by associated RVEs. In more detail, cracks of small opening in the cement phase are modelled by weak substitute material with Young's modulus of order 10^{-9} less than the cement paste (also compare experimental observations shown in Fig. 24). This procedure is of no practical consequence but preserves the mathematical foundation of the applied homogenisation method. Hereby, a designated transition zone, where the fibres and the matrix are disconnected, ensures correct material behaviour in the vicinity of the cracks (see e.g. Figure 27). The local macroscopic amount of damage is modelled depending on a criterion based on local von Mises stresses via different stages of RVE damage, characterised by zero to seven cracks of the cement matrix within the RVE (see Fig. 28).

The proof of principle is restricted to simulating a failure in the relevant part of the test specimen in a displacement-controlled tensile test as shown in Fig. 29.

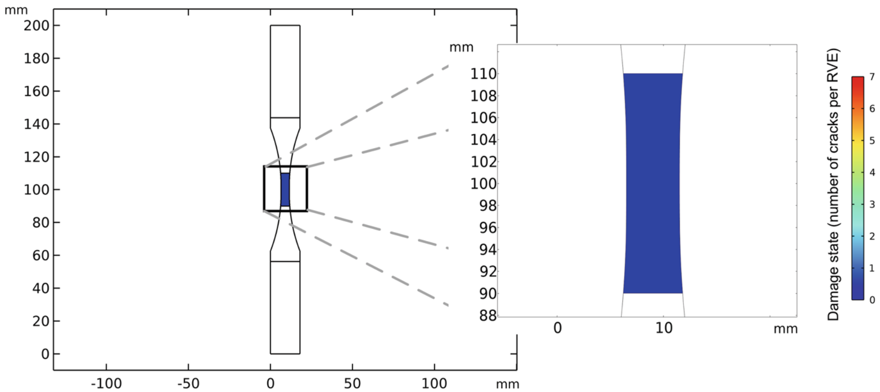

Fig. 29 Relevant part of the specimen for simulation (i.e. where cracks occur). The local number of cracks is depicted by the colour of the domain (here: 0 cracks everywhere at time 15 s)

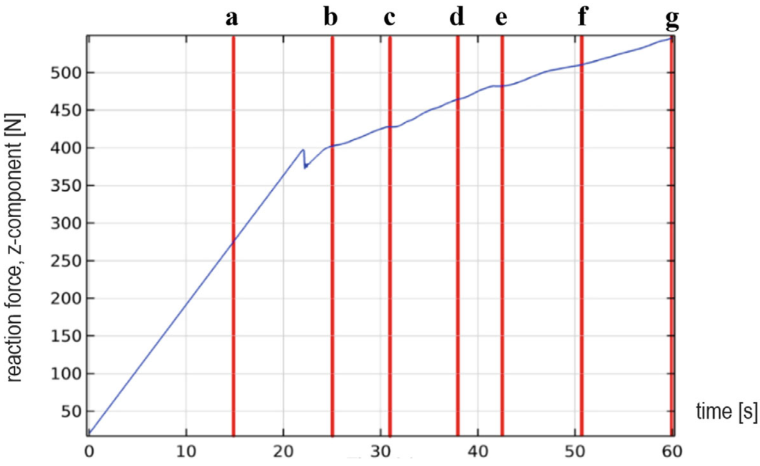

Fig. 30 Reaction force versus time. The red lines indicate, where the number of cracks in the relevant part of the sample are plotted in Figs. 29 (no crack) and 31b–g

4.3.2 Results

In the simulation of path-controlled tensile tests, the specimen is fixed at the lower part and the displacement is prescribed at the upper part following the experimental setup of the static tensile test. This results in the reaction force–time diagram depicted in Fig. 30. The graph shows at first a linear-elastic behaviour followed by several drops at different time steps, each connected by a linear material response.

Figure 31 shows the number of cracks in the relevant part of the sample (refer to Fig. 29) at different simulation times as indicated in Fig. 30. The combination of both figures implies that the drops happen as soon as the spread of the damaged zone associated with a certain no. of cracks extends across the entire specimen. Further, it can be seen that successive damage reduces the gradient of the curve, which corresponds to the strain-hardening like material response seen in the experiments.

5 General Conclusion, Outlook

Through extensive static and dynamic/cyclic (fatigue) testing series both on bending and tensile specimens of different scales, a wide range of valuable and new findings on the complex load-bearing, damage and failure behaviour of carbon short-fibre reinforced concrete (CSFRC) were gained. Strain-hardening of the material (and the transition to a non-linear stress–strain relationship) is achieved by the carbon fibres and their extremely good bond properties, leading to tiny microcracks and a very narrow crack spacing—providing a significant increase both in static/dynamic performance and flexural and tensile strength, respectively. Further, compared to

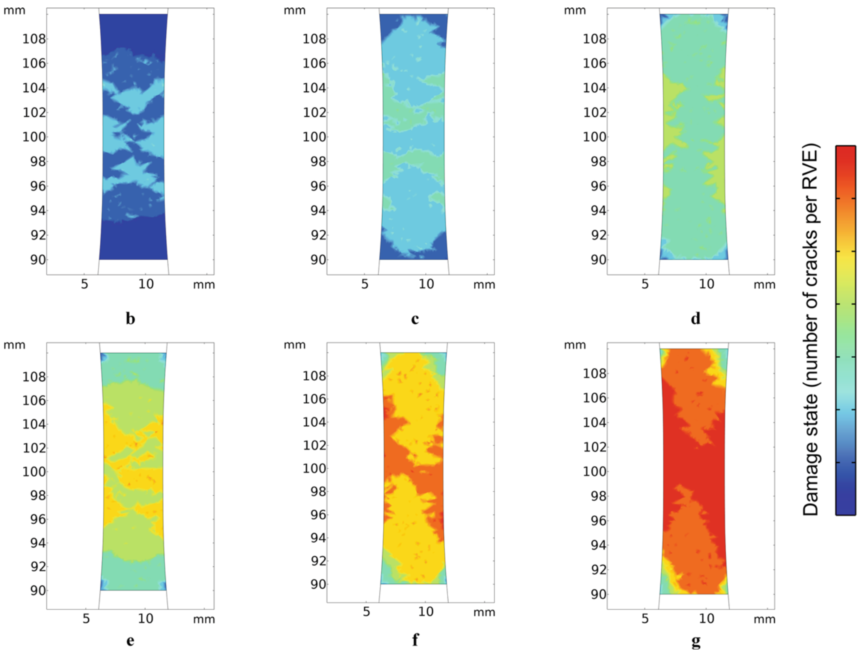

Fig. 31 No. of cracks at different simulation times: **b** 25 s, **c** 31 s, **d** 38 s, **e** 42.5 s, **f** 50.5 s, **g** 60 s

conventional steel fibres, the carbon fibres are already significantly activated in the un-cracked cross-section (i.e. before crack initiation at some 0.3–0.4‰).

Extensive NDT measurements (e.g. DIC, AE, electric sensors, X-ray CT, LDV, CWI, fibre-optics), including combined interpretations, significantly contributed to a deeper understanding of damage and fracture mechanisms. While DIC was primarily utilised to provide a sound overall survey of the (near-surface) damage and crack development, AE and electric measurements were particularly helpful to discriminate individual source types and to localise events, respectively—with different advantages/disadvantages dependent of the sample size and experimental setup. Further, ex-situ CT images were used to gain additional valuable information on the type of failure (fibre breakage or pull-out). Other techniques such as Coda Wave Interferometry (CWI) can help to indicate the progress of deterioration but has drawbacks in localisation and classification of defects. Lessons learned comprise information on best sensor positions, coupling, selection of sensors, and, in particular, frequency transfer functions of sensors.

The principle mechanical behaviour and structural damage as well as the damage development in cross-sectional areas under tension could be confirmed for all sample sizes/types and loading regimes (tension, flexure) with only minor differences. With regard to the specific type of failure, the static tests showed that the final specimen failure was initiated by progressive fibre breakage combined with fibre pull-out (i.e. bond/anchorage failure, especially of fibres with shorter bond length on one crack edge). In the cyclic fatigue tests, both damage evolution phase 2 (stable crack development) and phase 3 (unstable crack growth) could be observed across all loading types and scales, where the individual phases tended to be more pronounced and better identifiable with decreasing scale, particularly the generally very short phase 3. Thereby, the individual NDT measurements and their combinations suggest that phase 2 is mainly characterised by gradual fibre pull-out, while the final failure initiation in phase 3 seems to be primarily associated with fibre breakage. Within the additional fatigue tests with non-monotonous cyclic (varying) loading schemes on macro samples the results indicate tendencies towards sequence effects. Furthermore, it can be concluded that the specimens exhibit a more favourable fatigue behaviour under axial tension than with harmonic bending loading.

With regard to the mathematical multiscale modelling the results show that the developed model is capable of reproducing both the material behaviour and the relevant failure mechanisms. RVEs were derived from μ-CT and convergence tests determined the required RVE sizes and discretisation parameters, which turned out to give a numerically efficient computational model of the mechanical behaviour of the material. In combination with the experimental results, the model was then used to characterise the failure mechanisms. In particular, it was shown that the correlation between drops in reaction force and successive damage observed in the experiments can be reproduced by locally differently damaged RVEs related to different macroscopic crack densities associated with cracks in the concrete matrix and weakening of the surrounding fibre-matrix interface. Failure of the entire sample is finally caused by subsequent failure of the carbon fibres and/or fibre anchorage. Further refinement of the model like inclusion of pores or other macroscopic inhomogeneities or different sizes of the transition zones can be made straightforwardly if this level of detail is required. The cyclic tests generally show similar damage mechanisms as in the static domain. Therefore, by incorporating a specific fatigue parameter (taking into account the load/damage history) into the localised damage model developed, it is also possible to describe the failure process under cyclic loading in principle. However, an in-depth alignment beyond the investigations possible within the scope of the project with specific experimental fatigue data can contribute to develop further and calibrate generally the numerical model accordingly.

References

1. Hambach, M., Möller, H., Neumann, T., Volkmer, D.: Portland cement paste with aligned carbon fibers exhibiting exceptionally high flexural strength (> 100 MPa). Cem. Concr. Res. (2016). https://doi.org/10.1016/j.cemconres.2016.08.011
2. Hambach, M.: Hochfeste multifunktionale Verbundwerkstoffe auf Basis von Portlandzement und Kohlenstoffkurzfasern. Dissertation (2016)
3. Fischer, O., Volkmer, D., Lauff, P., Hambach, M., Rutzen, M.: Zementgebundener kohlenstofffaser-verstärkter Hochleistungswerkstoff (Carbonkurzfaserbeton). Bericht F 3178, BBSR, Fraunhofer (2019). ISBN 978-3-7388-0422-5

4. Lauff, P., Fischer, O.: Effizienter Ultrahochleistungsbeton mit innovativer trajektorienorientierter “Bewehrung.” Ce/papers **3**, 82–88 (2019)
5. Hambach, M., Volkmer, D.: Properties of 3D-printed fiber-reinforced Portland cement paste. Cem. Concr. Compos. (2017). https://doi.org/10.1016/j.cemconcomp.2017.02.001
6. Lauff, P.: Zur Herstellung und zum Trag- und Ermüdungsverhalten von Car-bonkurzfaserbeton. Dissertation, Technical University of Munich, in process
7. TUM: 3D Printing in Concrete—Additive Manufacturing at TUM. Online: https://www.youtube.com/watch?v=H3aD0VZ3ESU. Accessed 17 Mar 2021
8. Rutzen, M., Lauff, P., Niedermeier, R., Fischer, O., Raith, M., Grosse, C.U., Weiss, U., Peter, M.A., Volkmer, D.: Influence of fiber alignment on pseudoductility and microcracking in a cementitious carbon fiber composite material. Mater. Struct. **54**, 58 (2021). https://doi.org/10.1617/s11527-021-01649-2
9. Rutzen, M., Schulz, M., Mossburger-Will, J., Lauff, P., Fischer, O., Volkmer, D.: 3D printing as an automated manufacturing method for a carbon fiber reinforced cementitious composite with outstanding flexural strength (105 N/mm^2). Mater. Struct. **54**, 234 (2021). https://doi.org/10.1617/s11527-021-01827-2
10. Curosu, I., Liebscher, M., Mechtcherine, V., Bellmann, C., Michel, S.: Tensile behavior of high-strength strain-hardening cement-based composites made with high-performance polyethylene, aramid and PBO fibers. Cem. Concr. Res. (2017). https://doi.org/10.1016/j.cemconres.2017.04.004
11. Li, V.C., Leung, C.K.Y.: Steady-state and multiple cracking of short random fiber composites. J. Eng. Mech. (1992). https://doi.org/10.1061/(ASCE)0733-9399(1992)118:11(2246)
12. Li, V.C.: On engineered cementitious composites (ECC). ACT (2003). https://doi.org/10.3151/jact.1.215
13. Van Zijl, G.P.A.G., Wittmann, F.H.: On durability of SHCC. ACT (2010). https://doi.org/10.3151/jact.8.261
14. Lauff, P., Raith, M., Große, C., Rutzen, M., Volkmer, D., Reischmann, L., Weiß, U., Peter, M., Fischer, O.: Investigation of localised damage indicators of a carbon short-fibre reinforced high performance concrete under dynamic and flexural load. In: Proceedings of fib Symposium, Krakow/Poland, pp. 1952–1959 (2019)
15. Lauff, P., Pugacheva, P., Rutzen, M., Weiß, U., Fischer, O., Volkmer, D., Peter, M.A., Grosse, C.U.: Evaluation of the behavior of carbon short fiber reinforced concrete (CSFRC) based on a multi-sensory experimental investigation and a numerical multiscale approach. Materials **14**(22), 7005 (2021)
16. Rutzen, M., Volkmer, D.: Viscoelasticity and energy dissipation as indicators of flexural fatigue behavior in a ductile carbon fiber-reinforced cementitious composite. Int. J. Fatigue (2022). https://doi.org/10.1016/j.ijfatigue.2022.106839
17. Džolan, A., Lauff, P., Fischer, O., Šunjić, G.: Influence of concrete shrinkage on the behavior of carbon short-fiber-reinforced concrete (CSFRC) under tension. Appl. Sci. **13**(12), 7081 (2023). https://doi.org/10.3390/app13127081
18. Engelhard, M., Kalytta-Mewes, A., Volkmer, D.: Testing methods for deformation characterization on 3D printed carbon fiber reinforced cementitious composites. In: Proceedings of 14th fib PhD Symposium, Rome/Italy (2022)
19. Lauff, P., Fischer, O.: Damage indication by electrical resistivity measurement of carbon short fiber reinforced concrete in fatigue testing. In: Proceedings of the 13th fib International PhD Symposium in Civil Engineering (2021). ISBN 978-2-940643-11-0
20. Rutzen, M., Volkmer, D., Weiß, U., Reischmann, L., Peter, M.A., Lauff, P., Fischer, O., Raith, M., Große, C.: Microstructural analysis of crack growth caused by static and dynamic loads in a carbon fiber reinforced cement paste. In: Zingoni, A. (ed.) Proceedings of Advances in Engineering Materials, Structures and Systems: Innovations, Mechanics and Applications. CRC Press (2019)
21. Sause, M.G.: In-Situ Monitoring of Fiber-Reinforced Composites, vol. 242. Springer International Publishing, Cham (2016)

22. Schukraft, J., Lohr, C., Weidenmann, K.A.: 2D and 3D in-situ mechanical testing of an interpenetrating metal ceramic composite consisting of a slurry-based ceramic foam and AlSi10Mg. Compos. Struct. (2021). https://doi.org/10.1016/j.compstruct.2021.113742
23. Aggelis, D.G., Dassios, K.G., Kordatos, E.Z., Matikas, T.E.: Damage accumulation in cyclically-loaded glass-ceramic matrix composites monitored by acoustic emission. Sci. World J. **12**, 869467 (2013)
24. Gautschi, G.: AE sensors. In: Piezoelectric Sensorics: Force Strain Pressure Acceleration and Acoustic Emission Sensors Materials and Amplifiers, pp. 199–207 (2002)
25. Schumacher, T., Linzer, L., Grosse, C.: Signal-based AE analysis. In: Acoustic Emission Testing: Basics for Research—Applications in Engineering, pp. 73–116 (2022)
26. Grosse, C.U., Ohtsu, M., Aggelis, D.G., Shiotani, T. (eds.): Acoustic Emission Testing: Basics for Research—Applications in Engineering. Springer Nature (2021)
27. Sause, M.: Identification of Failure Mechanisms in Hybrid Materials Utilizing Pattern Recognition Techniques Applied to Acoustic Emission Signals. mbv Verlag (2019)
28. Sause, M.G., Gribov, A., Unwin, A.R., Horn, S.: Pattern recognition approach to identify natural clusters of acoustic emission signals. Pattern Recogn. Lett. **33**(1), 17–23 (2012)
29. Ospitia, N., Korda, E., Kalteremidou, K.A., Lefever, G., Tsangouri, E., Aggelis, D.G.: Recent developments in acoustic emission for better performance of structural materials. Dev. Built Environ. **13**, 100106 (2023)
30. Bian, C., Wang, J.Y., Guo, J.Y.: Damage mechanism of ultra-high performance fibre reinforced concrete at different stages of direct tensile test based on acoustic emission analysis. Constr. Build. Mater. **267**, 120927 (2021). https://doi.org/10.1016/j.conbuildmat.2020.120927
31. Wang, J.Y., Guo, J.Y.: Damage investigation of ultra high performance concrete under direct tensile test using acoustic emission techniques. Cem. Concr. Compos. **88**, 17–88 (2018). https://doi.org/10.1016/j.cemconcomp.2018.01.007
32. Ohtsu, M., Watanabe, H.: Quantitative damage estimation of concrete by acoustic emission. Constr. Build. Mater. **15**(5–6), 217–224 (2001). https://doi.org/10.1016/S09050-0618(00)00071-4
33. Van Steen, C., Verstrynge, E.: Signal-based acoustic emission clustering for differentiation of damage sources in corroding reinforced concrete beams. Appl. Sci. **12**(4), 2154 (2022). https://doi.org/10.3390/app12042154
34. Larisa, U., Solbon, L., Sergei, B.: Fiber-reinforced concrete with mineral fibers and nanosilica. Procedia Eng. **195**, 147–154 (2017)
35. Li, V.C., Wang, S., Wu, C.: Tensile strain-hardening behavior of polyvinyl alcohol engineered cementitious composite. ACI Mater. J. **98**(6), 483–492 (2001)
36. Gutkin, R., Green, C.J., Vangrattanachai, S., Pinho, S.T., Robinson, P., Curtis, P.: On acoustic emission for failure investigation in CFRP: pattern recognition, peak frequency analyses. Mech. Syst. Signal Process. **25**(4), 1393–1407 (2011)
37. Kravchuk, R., Landis, E.N.: Acoustic emission-based classification of energy dissipation mechanisms during fracture of fiber-reinforced ultra-high-performance concrete. Constr. Build. Mater. **176**, 531–538 (2018). https://doi.org/10.1016/j.conbuildmat.2018.05.039
38. Pomponi, E., Vinogradov, A.: A real-time approach to acoustic emission clustering. Mech. Syst. Signal Process. **40**(2), 791–804 (2013). https://doi.org/10.1016/j.ymssp.2013.03.017
39. Thum, F., Potstada, P., Sause, M.G.: Development of 25 kN in-situ load stage combining X-ray computed tomography & acoustic emission measurement. KEM (2019). https://doi.org/10.4028/www.scientific.net/KEM.809.563
40. Potstada, P.-E.: Konzeption und Durchführung von in-situ Computertomographie in der Anwendung auf Aluminiumlegierungen und Faserverbundwerkstoffe. Dissertation, Universität Augsburg (2021)
41. Schröder, J.: A numerical two-scale homogenization scheme: the FE2-method. In: Schröder, J., Hackl, K. (eds.) CISM Course 550, Plasticity and Beyond, pp. 1–64. Springer (2014). https://doi.org/10.1007/978-3-7091-1625-8_1
42. Raju, K., Tay, T.-E., Tan, V.B.C.: A review of the FE2 method for composites. Multiscale Multidiscip. Model. Exp. Des. **4**, 1–24 (2021). https://doi.org/10.1007/s41939-020-00087-x

43. COMSOL Multiphysics® 5.6. COMSOL AB, Stockholm. www.comsol.com
44. Cioranescu, D., Donato, P.: An Introduction to Homogenization. In: Oxford Lecture Series in Mathematics and Applications. Oxford University Press (1999)
45. Lochner, T., Peter, M.A.: Identification of microstructural information from macroscopic boundary measurements in steady-state linear elasticity. Math. Methods Appl. Sci. **46**, 1295–1316 (2023). https://doi.org/10.1002/mma.8581
46. Lochner, T., Peter, M.A.: Homogenization of linearized elasticity in a two-component medium with slip displacement conditions. J. Math. Anal. Appl. **483**, 123648 (2020). https://doi.org/10.1016/j.jmaa.2019.123648